THESIS FOR THE DEGREE OF LICENTIATE OF ENGINEERING

# Experimental and numerical studies of thermal radiation in gas, coal and co-fired pilot test facilities

ADRIAN GUNNARSSON

Department of Energy and Environment

CHALMERS UNIVERSITY OF TECHNOLOGY

Gothenburg, Sweden 2017

Experimental and numerical studies of thermal radiation in gas, coal and co-fired pilot test facilities

ADRIAN GUNNARSSON



Department of Energy and Environment
Chalmers University of Technology
SE-412 96 Gothenburg
Sweden
Telephone + 46 (0)31-772 1000

Printed by Chalmers Reproservice
Chalmers University of Technology
Gothenburg, Sweden 2017

Experimental and numerical studies of thermal radiation in gas, coal and co-fired pilot test facilities

ADRIAN GUNNARSSON
Division of Energy Technology
Department of Energy and Environment
Chalmers University of Technology

# Abstract

Throughout the industrialized era, fossil fuels have been used extensively in combustion processes to generate heat and electricity. However, the combustion of such fuels creates emissions of greenhouse gases, mainly carbon dioxide, and other hazardous products. As these gases are released to the atmosphere, they contribute to global warming, which is a global issue of concern. It is therefore of great importance to study combustion processes and explore new ways to reduce their environmental impacts. One way of reducing emissions of greenhouse gases is to replace the energy source: from fossil to renewable. To attain a better understanding of the combustion process experimental and modeling work is needed. Such work can be undertaken to increase the efficiency and demonstrate the possible effects of fuel substitution.

The first half of this thesis focuses on the rotary kiln process, which is used in iron ore pellet production, and studies the associated rotating furnace and the radiative heat transfer process. The experimental work was performed during a measurement campaign in a down-scaled version of the furnace, and the results are compared and modeled using a discrete transfer model for different fuels. The focus is on comparing a reference coal with co-firing cases that employ a combination of 70% reference coal and 30% biomass for two different types of biomass. The results reveal the possibility of using co-firing in a full-scale rotary kiln, which is not expected to have any significant impact on the radiative heat transfer within the process. Measurements from a similar but earlier campaign were used together with a radiative model, using the discrete ordinates method to study the process in three dimensions. While still under development, this model predicts trends when the operational conditions of the rotary kiln process are changed.

The second half of this thesis work focuses on soot formation in different propane flames. The combustion conditions were varied while the process stoichiometry was maintained, and soot formation was analyzed using two different measurement techniques. In the first campaign, the soot volume fraction was measured by gas extraction using a scanning mobility particle sizer (SMPS), together with a photo-acoustic soot spectrometer (PASS-3), to study the radiative properties of the soot particles. In the second campaign, the soot volume fraction was measured using laser-induced incandescence (LII) together with an extinction laser. In both campaigns, the radiative intensity was measured, and the different flames were modeled using a discrete transfer model of the radiative heat transfer. The differences between the modeled and measured radiative intensities were found to be small in both campaigns.

**Keywords:** Radiative heat transfer, rotary kiln, co-firing, soot volume fraction

# List of Publications

This thesis is based on the following papers:

I. A. Gunnarsson, D. Bäckström, R. Johansson, C. Fredriksson, K. Andersson, *Radiative Heat Transfer Conditions in a Rotary Kiln Test Furnace Using Coal, Biomass and co-firing Burners,* Submitted for publication in Energy and Fuels, 2017.

II. A. Gunnarsson, D. Bäckström, K. Andersson, J. Simonsson, M. Mannazhi, P. E. Bengtsson, *Measurements and Modeling of the Soot Volume Fraction in Propane Flames Using Laser Techniques and Radiative Heat Transfer Models,* Clearwater Clean Energy Conference 2017

III. D. Bäckström, A. Gunnarsson, D. Gall, X. Pei, R. Johansson, K. Andersson, R. K. Pathak, J. B. C. Pettersson, *Measurements of the Size Distribution, Volume Fraction and Optical Properties of Soot in an 80 kW Propane Flame,* Submitted for publication in Combustion and Flame, 2017.

IV. A. Gunnarsson, R. Johansson, K. Andersson, C. Fredriksson, *3D-Modelling of the Radiative Heat Transfer in a Rotary Kiln for Iron Ore Pellets Production,* Nordic Flame Days Conference 2016.

Adrian Gunnarsson is the main author of Papers I, III and IV and second author of Paper III. Dr. Daniel Bäckström, who is the main author of Paper III, has together with Dr. Robert Johansson and Professor Klas Andersson contributed with guidance in the modeling work, with discussions and editing of the papers. Dr. Christian Fredriksson acted as a contact person and was responsible for the planning of the experimental campaign at LKAB. Doctoral students Johan Simonsson and Manuu Mannazhi have together with Professor Per-Erik Bengtsson contributed with optical measurements during the experiments. Doctoral students Dan Gall and Xiangyu Pei, Associate Professor Ravi Kant Pathak, and Professor Jan B. C. Petterson have contributed with particle measurements during the experiments.

# Acknowledgements

First of all, I would like to thank my supervisors Klas Andersson and Robert Johansson for all the support and guidance you have given me throughout this work. I would also like to acknowledge my examiner Filip Johnsson for helping me into this interesting field of research.

Thank you Daniel Bäckström and Thomas Ekvall for your support during the experimental campaigns and for teaching me everything that I know about the oxy-fuel test rig. Thanks to Rikard Edland for the help and company during the many experimental hours. Johannes Öhlin, Rustan Hvitt and Jessica Bohwalli are greatly acknowledged for their help before, during and after the experimental campaigns. Johan Simonsson with co-workers and Dan Gall with co-workers are acknowledged for invaluable help with the measurements. Thanks to Christian Fredriksson for the great co-operation. I would specially like to thank Daniel, you always seems to have the time to answer my questions and share your knowledge. Whether it is concerning radiative heat transfer, experimental measurements or where to find the best triathlon equipment.

LKAB and the Swedish Energy Agency are acknowledged for the financial support of this work.

I would also like to thank Anna Köhler for sharing office with me and enthusiastically teaching me the most useful words found in the German language. Discussing with you is always a nice break in the work. Tove Karlsson, you have helped me countless of times, regardless the matter. We have followed each other since our first day at Chalmers and I hope that we can continue our journey for many years to come. To all my current and former colleagues at Energy Technology, thank you for creating such a pleasant working place.

I would also like to thank all my friends for being there for me and for filling my life with adventures. To Hilda, thank you for all your support during the last couple of months, for the countless laughs and your warm smile. Finally, I would like to thank my family that has always encouraged and supported me throughout the years.

Adrian Gunnarsson
Gothenburg, Sweden
April, 2017

# Table of Contents

*"....plus the fact that there may be literally millions of spectral lines, makes radiative transfer calculations a truly formidable task." – Michael F. Modest*

# Outline

This thesis consists of a summary of the work (ten chapters) and the four appended papers. The first two chapters provide a short background to the topics included in the thesis and describe what has previously been done in this area by our research group. Chapters 3 and 4 give descriptions of the test furnaces used in the different measurement campaigns and the different measurement techniques used. Chapter 5 describes the different radiation models used in the work for this thesis and the main equations of interest. Chapters 6 and 7 show some of the results, together with the associated discussions and conclusions from the work. The thesis ends with ideas for future work, a nomenclature and a bibliography.

Paper I assesses the possibility of using co-firing of coal and biomass in the grate-kiln process, which is used in iron ore pellet production. The radiative intensity and heat flux are measured, along with the gas temperatures, gas compositions, and particle concentrations in a 580-$kW_{th}$ cylindrical furnace. A discrete transfer model is used to model the radiative heat transfer, and the radiative heat profiles for different fuel combinations are compared. Papers II and III focus on the radiative heat transfer in different propane flames, wherein the soot volume fraction is measured using different measurement techniques. The radiative intensity is modeled using the discrete transfer model. In Paper II, the formation of soot is altered by changing the oxygen concentration in the oxidant for oxygen enriched air and oxy-fuel flames and laser-induced incandescence measurements of the soot volume fraction are performed together with an extinction laser. In Paper III, Scanning Mobility Particle Sizer (SMPS) spectrometry is used to measure the soot volume fractions for a non-sooty flame and a sooty flame. PASS-3 is used to study the optical properties of the soot particles. Paper IV evaluates the measurements obtained in an earlier campaign with the rotary kiln, and the radiative heat flux is modeled using the discrete ordinates method.

# 1. Introduction

A contemporary, important, global environmental challenge is to reduce emissions of greenhouse gases and hazardous substances from combustion processes. Combustion is commonly used in heat-requiring industrial processes or for electricity production in power plants. Chemically bound energy is released as heat in the combustion process as the fuel is converted with an oxidant, usually air, and combustion products are formed. The complete and desired combustion of hydrocarbon fuels and air results in the product gases of carbon dioxide and water, together with nitrogen. However, it is common for the fuel to contain different impurities, as well as for the combustion process to be incomplete, resulting in a flue gas that contains many different compounds. While greenhouse gases are linked to an increase in global warming other combustion products, such as soot particles, have more direct and negative effects on human health.

In the case of electricity production, the greenhouse gas emissions can be removed by exchanging the combustion process for processes that employ renewable energy sources, e.g., solar and wind power. Nonetheless, combustion processes remain important and necessary for many industrial processes, as well as for the global energy system. Alternatively, greenhouse gas emissions can be removed from combustion processes by replacing a fossil fuel with a fuel that is fully renewable, e.g., using biomass instead of coal. Co-firing a fossil coal and a renewable biomass means that a portion of the emissions originating from the fossil fuel is eliminated. Another approach is to capture the carbon ($CO_2$) emissions after the combustion process and store them (i.e., using carbon capture and storage techniques) to prevent the gases escaping into the atmosphere. Finally, emissions of greenhouse gases can be reduced by improving the efficiency of the combustion process. Moreover, by making the combustion process more efficient, the emission levels of other products (gases or particles) can be reduced.

To improve the combustion process it is necessary to understand how heat is transferred within the process. Heat transfer in a furnace occurs mainly through radiation if a flame is present, accounting for up to 90% of the total heat transfer in some processes [1]. The radiative properties of present gases and particles are complex but important to consider, since they contribute to the radiation through emission, absorption, and scattering. Therefore, it is of great interest to measure experimentally and model theoretically the radiative heat transfer for combustion processes.

Thanks to significant contributions from various research groups, such as Hottel & Sarofim [2], Siegel & Howell [3], Özisik [4] and Modest [5], research on radiative heat transfer in combustion systems has advanced rapidly since the 1960's. Based on the work of Modest [5] we built models for studying flame radiation in cylindrical enclosures, in which both gases and particles are considered. Our latest studies have investigated radiative heat transfer in coal and gas flames present in cylindrical furnaces, using different measurement methodologies and

modeling approaches for different applications, including oxy-fuel flames and rotary kilns[6]–[9].

This work studies the radiative heat transfer from flames, using a gaseous or solid fuel, in cylindrical furnaces. Roughly, half of this thesis work is focused on measurements and modeling of the radiative heat transfer for coal and co-firing flames in a down-scaled rotary kiln used for iron ore pellets production. The remaining part of the thesis studies the soot volume fraction and the radiative heat transfer for different propane flames in a cylindrical furnace using two different measurement techniques.

## 1.1 The Rotary Kiln Process

Iron ore is mined around the globe, with China, Australia, and Brazil being the three largest producers. Approximately 3,320 million tons of iron ore were mined in 2015, according to the 2016 USGS Mineral Commodity Summaries [10], with the steel industry being the primary user. After crushing and treating the ore, it is common for the mining companies to process the ore into a pelletized form to facilitate transportation, but also to achieve a good iron ore quality. A commonly used process to produce iron ore pellets is the so-called grate kiln process. Figure 1 shows a schematic of the grate-kiln process used by the Swedish mining company Luossavaara-Kiirunavaara AB (LKAB). Raw iron ore pellets are fed onto a travelling grate, where they are partially dried and oxidized from magnetite to hematite using hot air and flue gases that are passed through the bed and grate. From the grate, the iron ore pellets enter a rotary kiln with length of about 30 meters and diameter of about 5 meters. The kiln is slightly tilted and the burner, which is located at the center position at the lower end of the kiln, is continuously fed with fossil coal to sustain a long jet-like flame. As the pellets slide towards the lower end, they are further heated, oxidized, and sintered. Once they exit the rotary kiln, the pellets drop down into a rotating cooler. Ambient air is used in the four cooler zones (C1–C4). To exploit the heat from the pellets, the air leaving the cooler is transported to the grate zones (G2-G4) and kiln (Figure 1). Air leaving the first cooler zone, C1, is directed directly to the kiln, acting as preheated secondary air with a temperature of about 1200°C. In comparison to more-typical combustion processes, the volumetric flow of the secondary air flow is large to allow for oxidation of the pellets present in the kiln, with an oxygen content of about 16% in the flue gas. The flue gas leaving the kiln is directed through the pellets bed in zone G1. A more detailed description of a typical grate-kiln process can be found elsewhere [11].

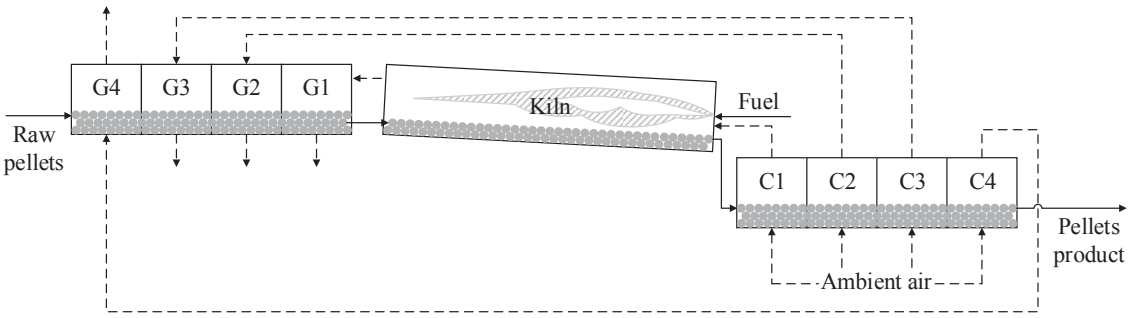


**Figure 1.** Schematic of the grate-kiln process used by LKAB. Raw iron ore pellets enter the grate at G4 and pass through the rotary kiln. The finished product exits the cooler section at C4.

A problem associated with iron ore pellet production is the continuous and substantial emissions of carbon dioxide generated from the combustion process, which are currently commonly fueled by fossil coal [1]. The choice of fuel is dictated mainly by the availability, composition, cost, and high heating value of the fuel. However, to reduce the impact on global warming of industries, the emission of greenhouse gases from the stationary industrial sector need to be drastically reduced. In the iron ore pellet industry, one way to achieve this might be to switch to less-carbon-intensive fuels. However, this might affect the heat transfer conditions in the rotary kiln, thereby compromising the quality of the product. To investigate this, modeling work can be performed using detailed radiation models. However, the radiative heat transfer that occurs during the rotary kiln process is complex and several different elements need to be considered. Heat is not only exchanged between the flame and the pellets, but also between the kiln wall and pellet bed. In the flame and in the furnace, gases and particles are present that emit, absorb, and scatter radiation, and this need to be considered in the modeling. Thermal radiation from the flame is anticipated to be dominated by hot particles, mainly char, but also ash and soot particles, since a solid fuel is used. The radiative heat transfer from solid fuel flames in cylindrical furnaces has been studied and modeled earlier [12]–[14], albeit for more conventional combustion conditions. Therefore, it is of interest to study how well the radiative heat transfer can be modeled in this process. Earlier modeling studies of the heat transfer in a rotary kiln [15]–[17] focused on the radiative and convective heat transfer of the gases in the freeboard and the surfaces of the kiln, while neglecting the particles present in the freeboard, which consist of unburned fuel, soot, and ash. There is currently a lack of quantitative knowledge of the heat transfer conditions in rotary kilns using any fuel, mainly due to the rotation of the kiln, which complicates in-flame measurements.

This thesis includes work that focuses on the radiative heat transfer within a rotary kiln and assesses the value of co-firing. The work includes measurements of radiative heat transfer performed in a down-scaled version of a full-scale rotary kiln, and the process is modeled using discrete transfer models and the discrete ordinates method (Papers I and IV).

## 1.2 Soot Formation

In combustion processes, soot formation at the flame occurs to different degrees depending on the combustion conditions applied, resulting in incomplete conversion of the fuel. The soot particles start to grow from heavy polycyclic aromatic hydrocarbons (PAH), which is followed by the absorption of different compounds from the surrounding gas phase and an increase in size due to collisions with smaller soot particles [18]. The combustion conditions affect the formation of soot; for example, the effect of varying the concentration of oxygen or carbon dioxide on soot formation has been examined by Du et al. [19] for ethylene and propane flames when adding the gas either premixed with the fuel or on the oxidizer side. Their goal was to examine separately the three major parameters that have impacts on soot formation, namely the dilution effect, thermal effect, and a direct chemical effect. They concluded that soot formation could be suppressed by the addition of carbon dioxide to either the fuel or the oxidizer side. The addition of oxygen revealed a more complicated relationship to soot formation and this is due to that oxygen addition influences kinetics (soot inception) as well as mixing and temperature conditions. In another study, conducted by Liu et al. [20], the formation of soot

and $NO_x$ was investigated while adding carbon dioxide to an ethylene flame. They investigated the formation mechanisms using detailed chemistry and transport properties in a numerical study. The authors concluded that the addition of carbon dioxide reduced the soot nucleation rate, as well as the rates of NO and $N_2O$ formation. The same effects were observed regardless of whether the gas was added on the fuel or on the oxidizer side, although the effect was more significant when the gas was added on the oxidizer side. The implicated reactions are R1 and R2:

$$CO_2 + H \leftrightarrow CO + OH \quad \text{R1}$$

$$CO_2 + CH \rightarrow CO + HCO \quad \text{R2}$$

The formed soot particles are small, often less than 10 nm in diameter [5], and they can travel long distances once emitted to the atmosphere. The particles are considered to be carcinogenic [21] and to cause premature deaths of people [22], making emissions of soot particles a health issue. Within the combustion process, the soot particles are of relevance from a heat transfer perspective, as they are an important contributor to heat radiation, given that they both emit and absorb radiation [23]. Thus, the heat transfer in a furnace is affected by the presence of soot particles. Any unexpected formation of soot may affect the performance of the furnace, with the consequence of increased operational cost. For these reasons, it is of interest to analyze the soot present in a furnace and model the radiative heat transfer in the process.

In the work for this thesis, the radiative intensities of different propane flames were measured and modeled, and the soot volume fraction was measured using two different techniques. In Paper II, non-intrusive measurements were conducted using an extinction laser together with a laser-induced incandescence system. In the work for Paper III, gas samples were extracted and the size distribution of the soot particles was determined using a scanning mobility particle sizer instrument. Radiative properties were also measured for the soot particles using a photo-acoustic soot spectrometer.

## 1.3 Aim and Scope

The overall aim of this thesis is to reveal the possibilities for performing measurements and detailed modeling work of radiative heat transfer in the grate-kiln process. In addition, coal-firing and co-firing with coal/biomass are compared in the process to evaluate the potential to lower greenhouse gas emissions by using renewable biomass instead of fossil coal. Two different models are used: a discrete transfer model and a model that applies the discrete ordinates method.

A parallel study is conducted on the soot volume fraction for different propane flames using different measurements techniques. Intrusive and non-intrusive measurements are made. By measuring the soot volume fraction, the radiative intensity can be modeled and compared to the experimental measurements.

# 2. Previous Work and Progress Made

The work presented in this thesis includes measurements and modeling of the radiative heat transfer for a down-scaled rotary kiln process used for iron ore pellet production, as well as for propane flames, investigating the soot volume fraction while varying the combustion conditions. Both of these areas have previously been investigated by our research group and the results obtained are briefly described and compared to the present work. For references to the different furnaces and measurement equipment, please see Sections 3 and 4, respectively.

## 2.1 Radiative Heat Transfer in a Rotary Kiln Test Furnace

A measurement campaign was carried out in 2013 by Bäckström et al. [9] in a cylindrical test furnace, which was built to resemble a full-scale rotary kiln. The aim of the work was to investigate the radiative heat transfer properties of different fuels under combustion conditions similar to those in a full-scale rotary kiln process. During the campaign, eleven different fuels or fuel combinations were tested, including two different coals, seven co-firing cases with coal and biomass, a heavy fuel oil, and finally, natural gas. One of the coals tested was a reference coal (RC) that is used on a daily basis at the full-scale rotary kilns in LKAB's production process. The second coal was a similar coal (SC) in terms of both chemical composition and size distribution. The co-firing cases were all conducted with the reference coal, although using three different biomasses, each tested at concentrations of 10% and 30%, based on the lower heating value. The three biomasses are here denoted as: biomass A (BA), being a wood treated with steam explosion; biomass B (BB), comprising grinded and pelletized wood; and biomass C (BC), which is a torrefied biomass. The co-firing cases were tested in a flexi-fuel burner. In the seventh co-firing case, biomass A was premixed with the reference coal (PM) and tested in the same coal burner as for the two coals.

During the experimental campaign, measurements of the temperature, gas composition, and radiative intensity were performed along the furnace axis, together with downstream particle extraction. The radiative intensity was measured using a narrow angle radiometer (NAR), and the results shown in Figure 2 are the values obtained at the second measurement port, 700-mm downstream of the burner. The NAR was traversed along the furnace diameter, entering at the inner wall of the furnace positioned at the 0-mm position. At the port entrance, high radiative intensities were measured owing to the high concentrations of particles and the high temperatures in the line-of-sight of the detector. As the probe was traversed closer to the center, the radiative intensity decreased in line with the total number of particles in the line-of-sight of the detector. At the opposite wall, located at a distance of 800 mm, the radiative intensity was close to zero due to the presence of a quartz window that was used as a cold background. Significant differences were observed with respect to the emitted flame radiation when different fuels were combusted in the test furnace, especially between the RC and SC, even though they appeared to be very similar in the fuel analysis (Figure 2a). These differences proved difficult to explain due to the lack of flame data. This was mainly due to problems with the particles clogging the suction pyrometer, preventing the achievement of a high suction velocity and

hindering accurate measurements of the flame temperatures. Furthermore, particle extraction was performed downstream of all the other measurements, which meant that particle data for positions close to the burner were lacking. The oil and gas flames were shorter than any of the solid fuel flames, as indicated by their low radiative intensity values (Figure 2b). This indicates that the heat load to the pellets in the full-scale rotary kiln would be rather different from that obtained using the reference coal. However, heavy fuel oil is used during the start-up phase of the full-scale process. The PM case and the co-firing case with 30% BA showed a slightly lower radiative intensity than the RC case (Figure 2c), while the other co-firing cases (BB and BC) appeared to have radiative intensity levels similar to that of the RC at the second measurement port (Figure 2d and e, respectively).

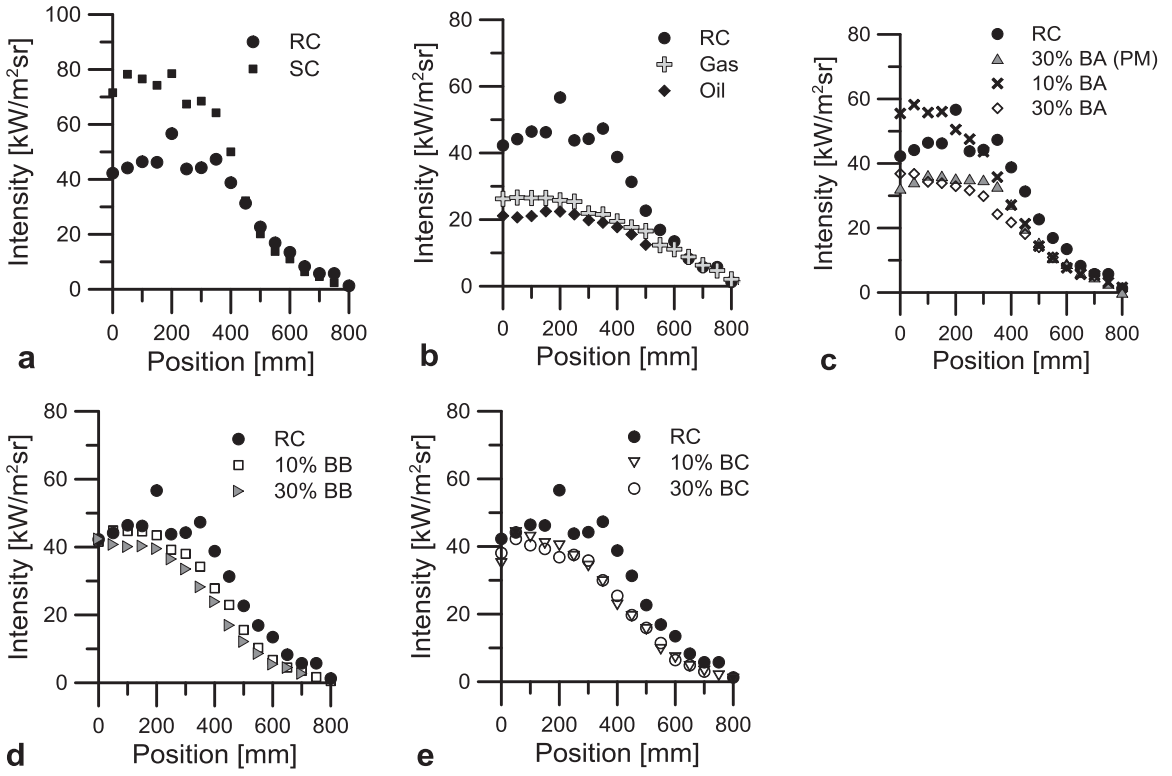


**Figure 2.** Radiative intensities measured 700-mm downstream of the burner, during the measurement campaign conducted in 2013 by Bäckström et al. [9] for two coals (RC and SC), gas, oil, and co-firing with three different biomasses (BA, BB, BC). The percentages corresponds to the portion of biomass in the co-firing cases.

Detailed radiation modeling was performed for the different cases, and it was found that all the co-firing flames were shorter than the coal-fired flames. In addition, it was shown by modeling that the heat transfer from the flame was dominated by the particles.

A second measurement campaign was performed in 2015, as described and discussed in Paper I of this thesis. The measurements were performed in a similar test furnace, with some modifications to ensure better process control and a new burner, which was installed to achieve more stable conditions with respect to biomass feeding to improve the quality of the experiments. The thermal input to the burner was increased from 400 $kW_{th}$ to 580 $kW_{th}$ and the furnace diameter was decreased from 800 mm to 650 mm. During this campaign, greater

emphasis was placed on co-firing flames, to examine the differences in temperature conditions and flame structure as compared to a coal flame. Compared to the 2013 campaign, the temperature measurements were superior, as extra care was taken to achieve and sustain a sufficient suction velocity using a new suction pyrometer and ejector system. Moreover, particles were sampled in the flame, close to the burner, and the radiative heat flux was measured. The radiative intensity was again measured and, using all the gathered data, the modeling was conducted with greater precision. Furthermore, the test matrix was increased with respect to the numbers of fuels and fuel combinations tested, as well as by introducing new measurement techniques, such as Fourier Transform Infrared Spectroscopy (FTIR) for gas analysis and an infrared camera for temperature estimations. The measurement campaign included the same reference coal, RC, and three new additional coals (C1, C2 and C3) as well as co-firing of the reference coal and the two different biomasses, BA and BB.

The burner configuration was changed at one point to resemble two different of LKAB's full-scale rotary kilns, KK2 and Svappavaara. The radiative intensity was again measured using the NAR at port MH3, located 1153 mm (KK2) or 933 mm (Svappavaara) from the burner, as shown in Figure 3. Similar profiles were achieved for the RC, C1, and C3 cases for the first burner configuration (Figure 3a). Much higher values were measured for the C2 case (Figure 3b), as also indicated by the very high temperatures. For the second burner configuration, similar values were measured for all three cases, indicating the possibility of using co-firing in the full-scale process (Figure 3c). However, in Paper I, only the Svappavaara configuration is considered and the paper focuses on the reference coal and the two co-firing cases for which 30% of the coal was substituted by biomass. The given percentage is based on the fuels' lower heating values while maintaining the total heat load to the burner.

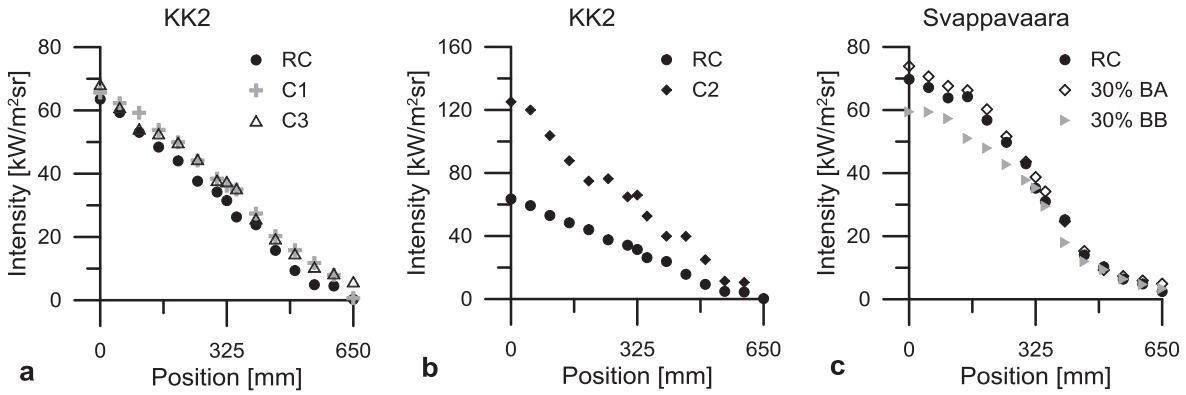


**Figure 3.** Measured radiative intensity at port MH3 during the campaign in 2015 (Paper I) for four different coals (RC, C1, C2 and C3) and two different co-firing cases (BA and BB). Two different burner configurations were tested with a varying distance to the burner of 1153 mm for KK2 (**a** and **b**) and 933 mm for Svappavaara (**c**). The percentages corresponds to the portion of biomass in the co-firing cases.

Detailed radiation modeling was performed also for these measurements, and good agreement was found between the measured and modeled total radiative intensities. However, some problems with condensing tars were encountered while extracting the particles from the co-firing flames, such that some of the data had to be discarded. This lack of data limited the

modeling work and highlights a problem that should be addressed in future measurement campaigns.

To date, the radiative heat transfer in the rotary kiln has been modeled using a detailed 1D radiation model, the discrete transfer model, and the results have been compared to measurements. In future work, a 3D model, which is currently under development and applies the discrete ordinates method, will be used to model the radiative heat transfer in the full-scale rotary kiln. Some early results derived using the 3D model are discussed in Paper IV.

## 2.2 Soot Formation in Propane Flames

Soot formation in the 80 kW propane flame was studied by Andersson et al. [24] in the Chalmers 100 kW oxy-fuel test rig equipped with a down-fired swirl-burner. Three different flames were studied; one flame using air as the oxidizer, and two oxy-fuel flames with oxygen concentrations of 21% and 27%, respectively. For all the experiments, the same stoichiometry was used ($\lambda$=1.15), which was achieved by varying the recycling rate of the dry flue gas and the addition of a corresponding amount of oxygen. Measurements of the temperature, total radiative intensity, and gas composition were performed. It was observed that the soot content initially decreased along with the flame temperature when the furnace operation was changed from air to oxy-fuel. However, with increased oxygen content in the recirculated flue gas, soot formation was again increased. No direct measurements of the soot volume fraction were performed. However, by comparing the measured and modeled gas and total radiative intensities, the soot particles could be identified to make up for the difference between the two values.

Subsequently, experiments were performed in the same test facility to estimate the soot volume fraction and study the optical properties of the soot [25], as described in Paper III. The 80 kW air-propane flame was used, and to produce soot particles, the primary air flow to the burner was adjusted using a valve. With the valve open, very few soot particles were observed; their number was lower than that seen previously in the work of Andersson et al. [24], likely due to the installation of a refractory burner quarl. Closing the valve resulted in the formation of soot particles. After particle extraction from the flame, the particle size distribution could be determined, and the soot volume fraction could be estimated using the Scanning Mobility Particle Sizer (SMPS). Simultaneous measurements of optical properties of the soot particles were estimated using a Photo Acoustic Soot Spectrometer (PASS-3) instrument. The soot absorption coefficients were compared to values calculated from refractive indices found in the literature with good agreements. The radiative intensity was also measured, and thereafter modeled using the measured soot volume fractions. The modeled intensities matched well with the measurements, and the soot volume fraction obtained with the SMPS spectrometer was considered reliable.

In the latest soot measurement campaign, described in Paper II, the same furnace was used with the same thermal input of propane to the burner. The cases studied in this work include air-propane flames, as well as cases in which the oxidant was varied by oxygen enrichment of the air or by operating the furnace in an oxy-fuel mode. In addition, cases were studied in which

low levels of NO or $SO_2$ were introduced into the oxidizer, and KCl (aq) was added using a probe and spraying the water solution into the flame. Finally, the air-propane flame was varied by varying the degree of opening of the valve to the primary air register. The soot volume fraction was measured in a collaboration with the Combustion Physics Department at Lund University of Technology, using optical and non-intrusive methods with a diode laser and a Laser-Induced Incandescence (LII) system. With this technique, it was possible to capture 2D images of the soot volume fraction along the diameter in the central part of the furnace using a CCD camera. The experimental set-up used in the latest campaign is shown in Figure 4. It was observed that soot formation was increased together with the oxygen content in the oxidizer for both the oxygen-enriched flames and the oxy-fuel flames. Detailed radiation modeling of the radiative intensity was performed with satisfying agreements being obtained.


**Figure 4.** Experimental set-up during the latest campaign (described in Paper II) showing the different components used to perform measurements of the soot volume fraction in the Chalmers 100 kW oxy-fuel test rig. Note that the diode laser is beneath the radiation shield and the laser beams are directed through the flame onto the detector.

# 3. Experimental Furnaces

For the experiments presented in this thesis, two different experimental furnaces were employed. Both furnaces are cylindrical but have different dimensions, are operated differently, and are used for different purposes. The two furnaces are: the experimental combustion furnace (ECF), which is located at LKAB in Luleå and the 100 kW oxy-fuel test rig located at Chalmers University of Technology in Gothenburg.

## 3.1 Experimental Combustion Furnace

Experiments to investigate the radiative heat transfer in the rotary kiln process were conducted in a cylindrical and refractory lined test furnace (Figure 5). The test furnace was constructed as a down-scaled version of a full-scale rotary kiln used in a grate-kiln process using constant velocity scaling. The furnace is tilted at an angle of 3° from the horizontal, with the burner positioned at the lower end. The burner axis is in line with the furnace axis, and the burner has six registers for primary air and fuel [26]. During the experiments, the burner was fed solid fuels, either pure coal or co-firing with coal and biomass, corresponding to a thermal input of 580 $kW_{th}$. Large volumes of preheated secondary air (about 2300 $Nm^3/h$) were introduced into two large registers, one above and one below the burner, as described previously [9]. In the first section of the test furnace, closest to and downstream of the burner, 13 measurement ports are located along the axis of the furnace, allowing for in-flame measurements. The ports are labeled MH0–MH12, and opposite side to the ports, quartz windows are placed to act as cold backgrounds when performing radiative intensity measurements. The first section has an inner diameter of 650 mm, widening to 800 mm for the second section. To resemble the pellet bed heat sink in the full-scale process, a cooling system is installed at the bottom of the furnace. Further details of the furnace and the different fuel cases tested in the furnace can be found in Paper I.

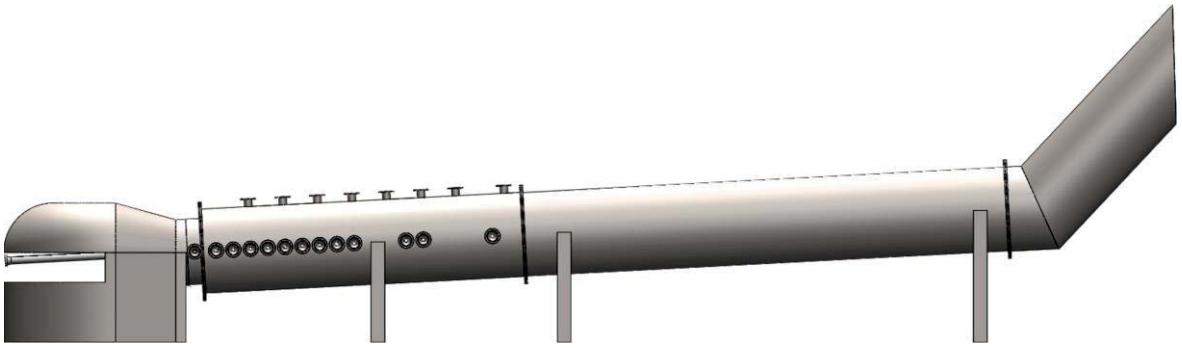

**Figure 5.** Schematic of the ECF used to study radiative heat transfer in the rotary kiln process. The thermal input to the burner is 580 $kW_{th}$ and the burner is placed to the left in the figure. Measurement ports that allow in-flame measurements are shown along the axis of the furnace (MH0-MH12).

A similar test furnace was used during the experimental campaign conducted by Bäckström et al. [9]. The two campaigns differed in that in the earlier campaign, the test furnace axis was horizontally lined with an inner furnace diameter of 800 mm along the whole axis, the thermal

input was lower at 400 $kW_{th}$, and there was no cooling section at the bottom of the bed. In addition, six extra measurement ports were installed. Some modeling of these measurements is performed in Paper IV. In both campaigns, the test furnace was stationary and empty of any bed material.

## 3.2 Oxy-Fuel Test Rig

Soot formation was studied in the Chalmers 100 kW oxy-fuel test rig (Figure 6a). The test rig, which is a cylindrical furnace that is down-fired with a swirl burner mounted on the top, can be used to study both gaseous and solid fuels. The fuel is introduced in the center of the burner and air enters through two annular swirling registers that have swirl angles of 45° and 15° for the primary and secondary air registers, respectively (Figure 6b). A refractory cone is located close to the burner to stabilize the flame. A more detailed description of the burner can be found in the report of Hjärtstam et al. [27]. The amount of oxidant that flows through each register can be altered by closing or opening the valve to either register. The inner diameter and height of the furnace are 800 mm and 2400 mm, respectively. Measurement ports (M) are located at different axial distances from the burner, or levels, allowing for in-flame probing, as well as access for optical measurements. Four measurement ports are available at each level, being equally spaced along the circumference of the furnace. Four water-cooled tubes are present in the furnace, cooling the flame to temperatures close to those seen in more conventional combustion processes. The test rig can be operated to allow for the recirculation of flue gases, and through the addition of oxygen, it can be operated in an oxy-fuel mode, replacing the nitrogen in the air with carbon dioxide from the combustion. Injections of different compounds to the oxidant, such as NO or $SO_2$, or the addition of water solutions of salts to the flame through the MS port are also possible, allowing studies of the effects of such additives.

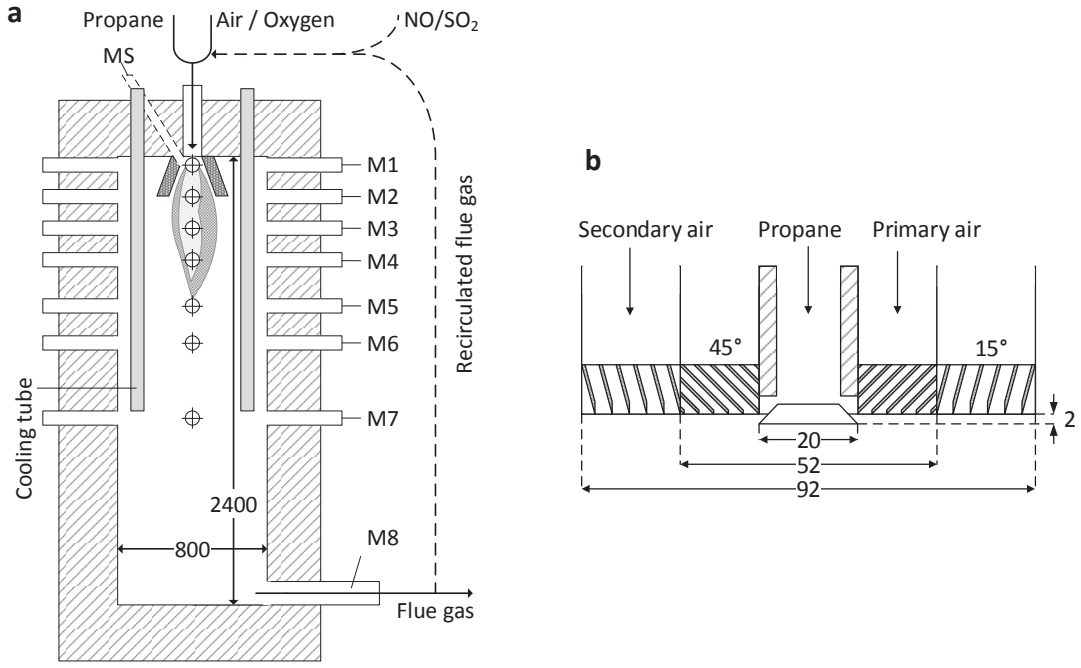


**Figure 6. a** Schematic of the Chalmers 100 kW oxy-fuel test rig. Measurement ports (M) are located along the axis of the furnace. **b** Cross-section of the burner showing the propane flow in the center of the burner and the primary and secondary air registers with their respective swirl angles. Dimensions are given in millimeters.

# 4. Measurement Techniques

To understand the radiative heat transfer in the two test furnaces, measurements of different parameters are made. This is ideally achieved by disturbing the flame as little as possible using non-intrusive methods. However, this is not always possible, and for some parameters, intrusive methods must be used. The measurement techniques used in this work are described below, together with schematics of the measurement equipment.

## 4.1 Intrusive Measurements

### *4.1.1 Narrow angle radiometer*

The radiative intensity was measured along the furnace diameter using a narrow angle radiometer (NAR) (Figure 7), which is an instrument that has been used in several studies by our research group, e.g. [8], [9], [24], [28]. This water-cooled probing instrument is equipped with a thermopile detector at the back end of the probe. Incoming light is focused on the detector, the voltage across the detector is measured, and the signal corresponds to the radiative intensity, which is calibrated to a high-precision black-body furnace before the start of the campaign. To reach the detector, the incoming light has to travel approximately 2.3 m along the water-cooled probe, which has an inner diameter of 1 cm. Thus, light rays that originate exclusively from a narrow angle to the detector's normal will reach the detector, and the instrument can be considered to measure only the radiative intensity in its line-of-sight. Most of the background radiation (from, for example, a hot furnace wall) can be removed if the probe is directed to a cold background, such as a quartz glass. To minimize the bending due to high flame temperatures, the probe is made from titanium. A small flow of nitrogen is used in the ray path to prevent any absorbing $CO_2$ or $H_2O$ entering the probe. To maintain a constant temperature for the detector, separate cooling systems are applied to the probe and the detector house. The NAR was used for the measurements reported in Papers I-IV.

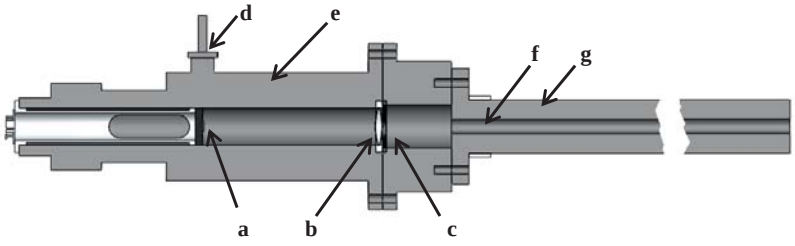


**Figure 7.** Schematic of the narrow angle radiometer that was used to measure the total radiation intensity. The probe includes the following components: **a** thermopile; **b** focusing lens; **c** shutter; **d** PT-100; **e** water-cooled sensor housing; **f** collimating tube; and **g** water-cooled probe.

### *4.1.2 Suction pyrometer*

Accurate measurements of the flame temperature are difficult to perform. When a thermocouple is used, an error will occur due to radiative influences. Consider a simple case in which the surrounding walls have a lower temperature than the position of interest in the flame. Ignoring

any absorption of radiation by the gas, a simple energy balance across the thermocouple can be expressed as:

$$A_{tc}h\left(T_{flame} - T_{tc}\right) = A_{tc}\varepsilon\sigma(T_{tc}^4 - T_{wall}^4) \quad (1)$$

That is, a temperature that is lower than the actual flame temperature, $T_{flame}$, will be measured by the thermocouple, $T_{tc}$, in this example due to the radiative heat losses to the surrounding walls, $T_{wall}$. The measurement error may, however, be reduced by increasing the convective heat transfer coefficient, $h$, from the flame to the thermocouple. Applying suction around the thermocouple increases the gas velocity and thus increases the value of $h$. The radiative heat loss can be decreased further by shielding the thermocouple, which means radiative heat exchange will instead occur between the thermocouple and the shield and between the shield and the walls. Such an instrument is called a suction pyrometer, and it is common to use a single shield for a gaseous flame, as in Papers II and III, and a triple shield for a solid fuel flame, as in Papers I and IV. Figure 8 shows a schematic of a triple-shielded suction pyrometer of IFRF type attached to a water-cooled probe. A type B thermocouple was used for all the measurements in this work. However, the applied suction to the suction pyrometer affects the gas flow pattern of the flame. Furthermore, the increased suction velocity reduces the measurement error, although the volume from which the gas is extracted also increases, and the measurement will not be a point measurement. That is, the suction velocity should be sufficiently high to minimize the measurement error but low enough to be considered a point measurement. A problem that can occur while performing measurements with this instrument is that the suction line becomes clogged with heavy particle loads or ash melts.

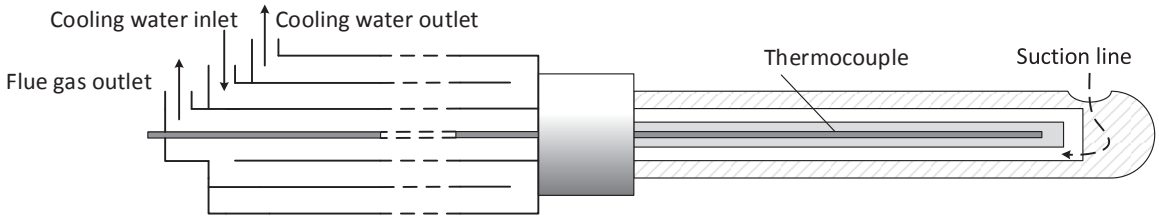


**Figure 8.** Schematic of a triple shielded suction pyrometer connected to a water-cooled probe. Gas is sucked through a hole in the outer most shield and then passes through the middle and inner most shield. The thermocouple is protected from the gas by the inner most shield.

### *4.1.3 FTIR for gas composition measurements*

In combustion, the two gas components of greatest significance are $CO_2$ and $H_2O$, considering their absorption and emission properties as well as expected high concentrations. In this work, gas was extracted from the furnace using a probe, and the gas was analyzed using FTIR. The absorption values at different wavelengths are measured in a small cell, and Fourier transforms are used to convert the measured absorption to spectra, which are compared to a database that contains a high number of components. For more details on the FTIR instrument and technique, see e.g. the work of Griffiths and Haseth [29]. To protect the probe itself from become damaged by the high flame temperatures, it is usually water-cooled. However, it is important that the extracted gas does not become too cool, since the water vapor would start to condensate. To avoid this, the inner tube is electrically heated to maintain the gas entering the FTIR at a

temperature of about 200°C. If the extracted gas is from a solid fuel flame, large amounts of particles are present, and a filter must be placed at the tip of the probe to avoid choking the system and to protect the FTIR from particles (Figure 9). The filter used in this work was composed of sintered alumina oxide. For a gas flame, such filters are normally not required, as very few particles are present, although a filter may still be useful if a very sooty flame is probed. A gas extraction probe was used in Papers I-IV.

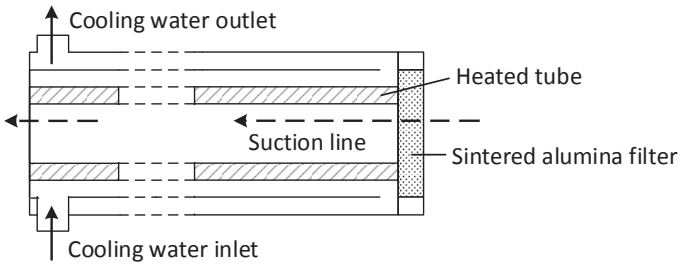


**Figure 9.** Water-cooled gas extraction probe with a sintered alumina filter at the tip. Electrical heating is applied to an inner tube, preventing the condensation of water from the gas sample.

### *4.1.4 Particle extraction probe*

The concentration and size distribution of the particles were measured by extracting samples from the flame. This was accomplished using a probe that was connected to a low-pressure impactor with thirteen sizing steps, ranging from 30 nm to 10 µm. Particles of diameter >10 µm were captured in a cyclone that was placed before the impactor. The opening for particle sampling was located perpendicular to the probe axis and was directed towards the burner (Figure 10). The gas sample was then diluted with nitrogen in the tip of the probe to quench any reactions and the overall dilution rate could be estimated by comparing the oxygen concentration in the diluted sampling gas with the oxygen concentration at the measurement position. This probe type was used to collect fuel, ash, and soot particles in Papers I and IV.

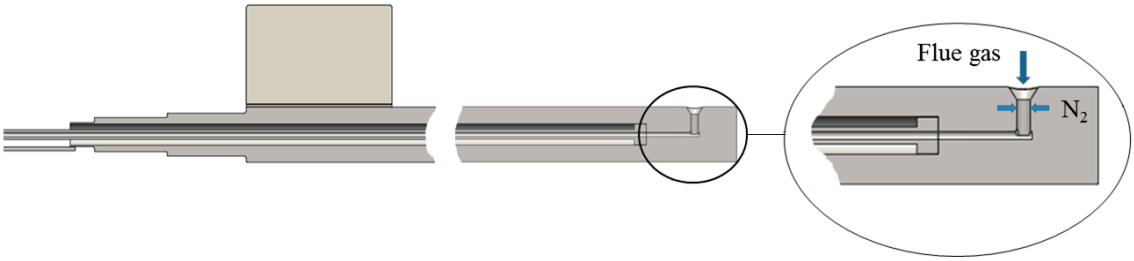


**Figure 10**. Particle extraction probe used to collect in-flame particles. The opening is directed orthogonally to the probe suction line, and the sample gas is diluted with nitrogen in the tip of the probe.

It is worth mentioning here that it is very complicated to measure particle distribution in an accurate way. To disturb the flow as little as possible, it is desirable to perform the particle extraction isokinetically, i.e., sampling the particles using a suction velocity that is equal to the flame velocity. However, it has been shown in earlier works using similar probes that accurate measurements do not require that the sampling is perfectly isokinetic, e.g., the work of Zhang et al. [30]. Moreover, a high particle load has the undesired effect of clogging the probe, even more so if the fuel is biomass, in which case tars condense in the probe.

*4.1.5 SMPS*

Soot particles were extracted from the flame and studied with a Scanning Mobility Particle Sizer (SMPS) [31] (Figure 11). The instrument provides the size distribution with high resolution for particles smaller than 1 µm, and is more commonly used for atmospheric measurements. Particles are charged by a radioactive source in the first step and then, by applying a voltage over the gas, separated with respect to their different electrical motilities in a Differential Mobility Analyzer (DMA) [32]. In a second step, the particles are counted in a Condensational Particle Counter (CPC). This measurement technique was used in Paper III.

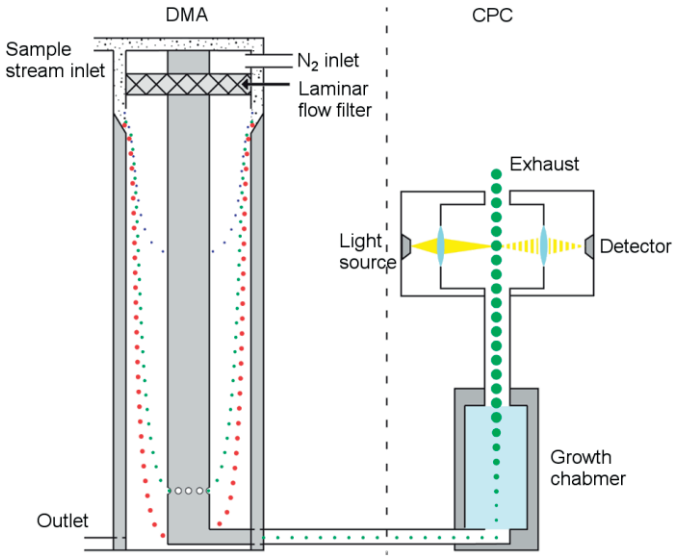


**Figure 11.** Schematic of the scanning mobility particle sizer (SMPS) used to measure the particle size distribution of soot.

*4.1.6 PASS-3*

A Photo-Acoustic Spectrometer (PASS-3) was used in Paper III to measure the absorption and scattering coefficients of the soot particles (Figure 12). Gas was extracted from the flame, and lasers of three different wavelengths were applied to the sample gas. A simple explanation of the theory behind this is that the particles absorb the laser energy and become heated and as the heat is transferred to the surrounding gas, a sound wave is produced, which is measured by a microphone. The sound wave is then correlated to the particle absorption. The scattered light is measured in a nephelometer. For more details on the PASS-instrument see e.g. the review work of Moosmüller et al. [33].

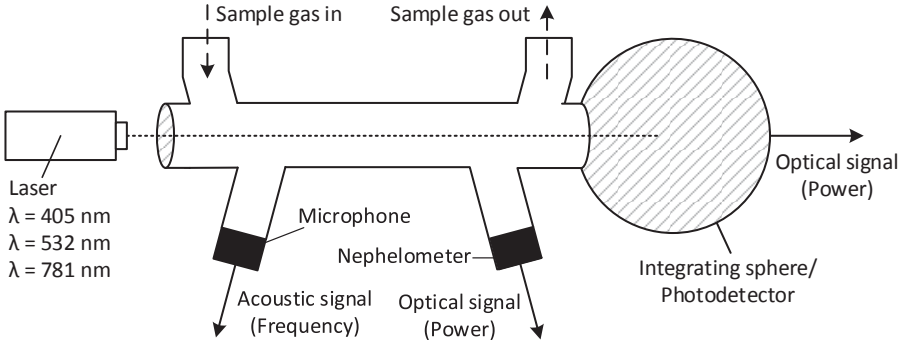


**Figure 12.** Schematic of the PASS-3 instrument used to measure the absorption and scattering coefficients of soot particles.

## 4.2 Non-intrusive Measurements

### *4.2.1 Ellipsoidal radiometer*

The radiative heat flux can be measured in a non-intrusive way if it is measured only at the inner wall of the furnace. In this work, the radiative heat flux was measured using an ellipsoidal radiometer placed in the tip of a probe, with a view angle of about 2π sr (Figure 13). Placing the tip of the probe in line with the furnace wall, the radiative heat transferred from the whole furnace to a small point on the furnace wall is measured. This instrument was used in Paper I.

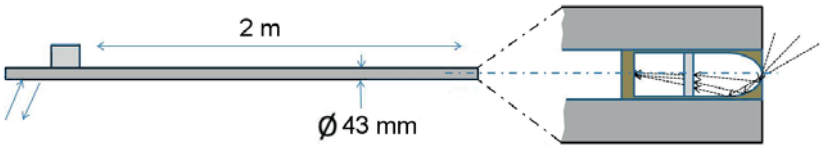


**Figure 13.** Schematic of the ellipsoidal radiometer used for measuring the radiative heat flux to the furnace wall

### *4.2.2. Infrared measurements*

It may be desirable to visualize the flame and the flows of gases and solids in a combustion process. While any camera could be used for this, if it is also of interest to study the temperature in the furnace an infrared camera can be used. A FLIR A655SC infrared camera with the possibility to measure temperatures up to 2000°C at a sampling frequency of 200 Hz and with a resolution of 640×120 pixels was used at the ECF. The camera was placed outside the furnace ports and was protected by a cooling house. The recorded videos were analyzed using the FLIR Research IR Max software (Paper I). Figure 14 shows example of images acquired along the ECF furnace axis from the camera for a coal flame.

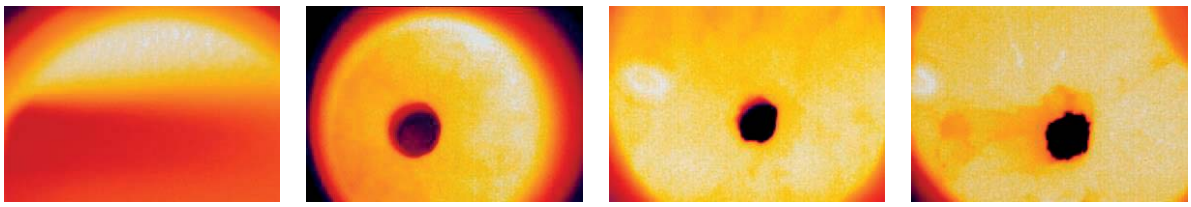

**a** **b** **c** **d**

**Figure 14.** Representative images acquired by the infrared camera for a coal flame, showing the interior of the furnace with hot gases and particles. The suspension flow moves from the left to the right in the panels, with **a** being close to the burner and **b**, **c** and **d** being located progressively downstream of **a**. Particles can be observed as denser fields that are passing the ports.

### *4.2.3 Laser equipment*

The in-flame soot volume fraction was estimated in Paper II using a diode laser together with the LII system. The diode laser was used to measure the extinction through the flame at a wavelength of 808 nm and used to calibrate the LII-signal. The LII-signal is captured using an intensified CCD camera, capturing 2D images from the Nd:YAG laser sheet at 1064 nm introduced to the furnace. The soot particles absorb the laser energy, are rapidly heated to their sublimation temperatures of 3500 - 4000 K, and start to emit black-body radiation. The particles maintain a much higher temperature than the surroundings at this point, and the emitted

radiation, i.e., the incandescence, is easily captured [34] by the camera placed orthogonally to the laser sheet. A simplified schematic of the laser and detector arrangement is shown in Figure 15. The two lasers were directed to pass through the same part of the flame, although the measurements were not performed simultaneously to avoid signal interference.

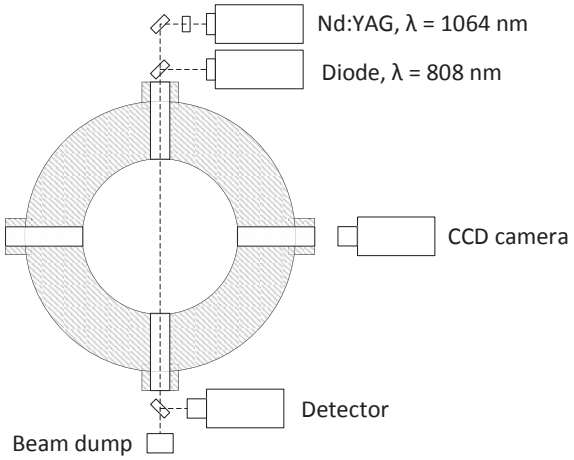


**Figure 15.** Simplified schematic of the laser set-up used in Chalmers 100 kW oxy-fuel test rig with a diode laser and the LII system.

The soot volume fraction is estimated by converting the LII-signal to quantitative 2D soot volume fractions [35], [36]. An averaged soot volume fraction is calculated over an absorbing path length $L$ where soot particles are present, estimated from the two-dimensional images, using the incident, $I_0$, and transmitted intensities, $I$, as follows:

$$f_v = \frac{\lambda_d}{6\pi L E(m_\lambda)} \ln\left(\frac{I_o}{I}\right) \tag{2}$$

where $f_v$ is the volume fraction of soot, $\lambda_d$ is the wavelength of the diode laser, and $E(m_\lambda)$ is a function of the complex refractive index of soot $m_\lambda$ [see Eqns. (13) and (18)]. An average of the LII-signal along the diameter of the flame is calculated, and given that the soot volume fraction is roughly proportional to the LII-signal [37], the soot volume fraction in each pixel of the 2D image can be estimated.

# 5. Radiation Modeling

It is of interest to study the radial intensity profiles of flames to reach a better understanding of the combustion process. To calculate the radiative intensity along the furnace diameter, i.e., along one direction $\hat{s}$ the radiative transfer equation (RTE) has to be solved. The RTE describes the change in intensity as the sum of the contributions from emissions, absorption, and scattering away from and in the $\hat{s}$ direction. For a given wavenumber, $\nu$, the RTE can be written as:

$$\frac{dI_\nu}{ds} = \kappa_\nu I_{b\nu} - (\kappa_\nu + \sigma_{s\nu})I_\nu + \frac{\sigma_{s\nu}}{4\pi}\int_0^{4\pi} I_\nu(\hat{s}_i)\Phi_\nu(\hat{s}_i, \hat{s})d\Omega_i \tag{3}$$

where $\kappa$ and $\sigma$ are the absorption and scattering coefficients, respectively, $\hat{s}_i$ is the direction of intensity being scattered into the $\hat{s}$ direction, and $d\Omega_i$ is the solid angle of the small ray in the $\hat{s}_i$ direction. The scattering phase function, $\Phi_\nu$, describes the probability that a ray from the $\hat{s}_i$ direction will be scattered into the $\hat{s}$ direction [5]. The absorption coefficient is dependent upon both the gases and particles in the line of a ray of light, while the scattering coefficient is related to the presence of particles.

## 5.1 Gas Radiation

When performing calculations of the radiative heat transfer, it is important to consider any gases that are present in the pathway of a ray of light. The gas may absorb or emit radiation to different degrees depending on the gas composition and temperature. However, if the medium consists of a pure gas without particles, the scattering may be neglected, as the gas molecules are much smaller than any wavelengths of interest [5], thereby simplifying the RTE to:

$$\frac{dI_\nu}{ds} = \kappa_\nu I_{b\nu} - \kappa_\nu I_\nu = \kappa_\nu(I_{b\nu} - I_\nu) \tag{4}$$

As shown in Eqn. (4), the absorption coefficient is dependent upon the wavenumber. Thus, these calculations require knowledge of the spectral properties of the gas. In combustion processes, the gases of the greatest importance are water and carbon dioxide. The absorption and emission of radiation by these gases differ for different wavenumbers. The RTE can be solved for each spectral line by performing line-by-line calculations. However, these calculations are computationally cumbersome and cannot be reasonably applied in other than very simple cases. If the system instead is complicated, as in CFD models, a more simple gas model can be utilized, e.g., a global gray gas model. However, other approaches exist that are intermediate to these two models considering the model complexity, accuracy, and how computationally demanding they are, i.e., narrow- or wide-band models.

### *5.1.1 Weighted-sum-of-gray-gases model*

An approach to modeling the radiative properties of gases is the weighted-sum-of-gray-gases (WSGG) model, as first presented by Hottel and Sarofim [2]. The model assumes the gas mixture in the furnace to be a mixture of a number of gray gases. Each gray gas has a fixed

absorption coefficient depending on the molar ratio of water steam and carbon dioxide. That is, each gas represents all the spectral regions with an absorption coefficient in a specific range and may be calculated according to Eqn. (5). In the spectral regions where the gases neither emit nor absorb, the radiation is represented by a so-called clear gas for which the absorption coefficient is set at zero, $\kappa_0 = 0$.

$$\kappa_j = \mathrm{K1}_j + \mathrm{K2}_j \frac{Y_{H_2O}}{Y_{CO_2}} \tag{5}$$

Depending on the same molar ratio but also the gas temperature, the weights for each gas are calculated, corresponding to the fraction of the black-body radiation belonging to each gas. Including the weight for the clear gas, the sum of the weights is equal to one.

$$a_j = \sum_i c_{j,i} \left( \frac{T}{T_{ref}} \right)^{i-1}$$

$$a_0 = 1 - \sum_{j=1}^{J} a_j \tag{6}$$

$$c_{j,i} = C1_{j,i} + C2_{j,i} \frac{Y_{H_2O}}{Y_{CO_2}} + C3_{j,i} \left( \frac{Y_{H_2O}}{Y_{CO_2}} \right)^2$$

The coefficients required to calculate the absorption coefficients and weights for the gray gases are given in Table 1 for a modified WSGG model derived from the work of Johansson et al. [38]. The modified version of the WSGG model was developed for molar ratios in the range of 0.125–2, temperatures in the range of 500 – 2500 K, and pressure path lengths in the range of 0.01–60 bar m, for a set of one clear and four gray gases.

**Table 1.** WSGG-model coefficients for each of the four gray gases, *j*, derived from the work of Johansson et al. [38]

| $j$ | 1 | 2 | 3 | 4 |
|---|---|---|---|---|
| $\mathrm{K1}_j$ | 0.055 | 0.88 | 10 | 135 |
| $\mathrm{K2}_j$ | 0.012 | -0.021 | -1.6 | -35 |
| $\mathrm{C1}_{j,1}$ | 0.358 | 0.392 | 0.142 | 0.0798 |
| $\mathrm{C1}_{j,2}$ | 0.0731 | -0.212 | -0.0831 | -0.0370 |
| $\mathrm{C1}_{j,3}$ | -0.0466 | 0.0191 | 0.0148 | 0.0023 |
| $C2_{j,1}$ | -0.165 | -0.291 | 0.348 | 0.0866 |
| $\mathrm{C2}_{j,2}$ | -0.0554 | 0.644 | -0.294 | -0.106 |
| $\mathrm{C2}_{j,3}$ | 0.0930 | -0.209 | 0.0662 | 0.0305 |
| $\mathrm{C3}_{j,1}$ | 0.0598 | 0.0784 | -0.122 | -0.0127 |
| $\mathrm{C3}_{j,2}$ | 0.0028 | -0.197 | 0.118 | 0.0169 |
| $C3_{j,3}$ | -0.0256 | 0.0662 | -0.0295 | -0.0051 |

Neither the absorption coefficient nor the weight is dependent upon the pressure path length, although the total emissivity of the gases is.

$$\varepsilon = \sum_{j=0}^{J} a_j (1 - \exp(-\kappa_j PS(Y_{CO_2} + Y_{H_2O}))) \tag{7}$$

Using the WSGG model, the RTE may be expressed as:

$$\frac{dI_j}{ds} = \kappa_j \left( [a_j I_b] - I_j \right) \tag{8}$$

*5.1.2 Statistical-narrow-band model*

A more detailed approach to estimate gas radiation is to use a statistical-narrow-band (SNB) model. In the SNB model, actual absorption coefficients for each spectral line are replaced with the averaged values for narrow spectral bands, together with random spacing and the strength of the spectral lines. To enable statistical treatment of the bands, the spectrum has to be divided into bands that are sufficiently wide to contain many lines, but narrow enough to assume constant black-body radiation in the band [38]. Different probability functions have been developed, for example by Goody [39] and Malkmus [40] , to generate realistic representations of the varying line strengths, $S_l$. Malkmus [40] gives that:

$$p(S_l) = \frac{1}{\bar{S}_l} \exp\left( -\frac{S_l}{\bar{S}_l} \right), \qquad 0 \le S_l < \infty \tag{9}$$

In the present work, the SNB model of Malkmus has been used, since for polyatomic molecules it is recognized as the best model currently available [5]. Using the Malkmus SNB model, Soufiani and Taine calculated temperature dependent narrow band parameters, $d_k$ and $k_k$, for $H_2O$, $CO_2$ and CO [41], which were later updated with additional parameters for $CH_4$ by Rivière and Soufiani [42]. The spectrally averaged transmissivity of a narrow band $k$ with a bandwidth $\Delta\nu$ of 25 $cm^{-1}$ is calculated for a gas ($g$) as follows:

$$\bar{\tau}_{\nu_k, g} = \exp\left[ -\frac{2\gamma_g}{d_k} \left( \sqrt{1 + \frac{Y_g PS k_k d_k}{\gamma_g}} - 1 \right) \right] \tag{10}$$

Only the water steam and carbon dioxide are considered in this work, and the mean line half-widths for these two gases are given as:

$$\gamma_{H_2O} = \frac{P}{P_{ref}} \left\{ 0.462 Y_{H_2O} \left( \frac{T_{ref}}{T} \right) + \left( \frac{T_{ref}}{T} \right)^{0.5} \left[ 0.079 \left( 1 - Y_{CO_2} - Y_{O_2} \right) + 0.106 Y_{CO_2} + 0.036 Y_{O_2} \right] \right\} \tag{11}$$

$$\gamma_{CO_2} = \frac{P}{P_{ref}} \left( \frac{T_{ref}}{T} \right)^{0.7} \left\{ 0.07 Y_{CO_2} + 0.058 \left( 1 - Y_{CO_2} - Y_{H_2O} \right) + 0.1 Y_{H_2O} \right\}$$

The total transmissivity, for all the present gases, may be calculated as the product of the transmissivity values of the separate gases:

$$\bar{\tau}_{\nu_k,tot} = \prod_g \bar{\tau}_{\nu_k,g} \tag{12}$$

In those cases in which the pathway is neither isothermal nor homogeneous, the Goody-Godson [5] approximation is used.

## 5.2 Particle Radiation

The combustion of solid fuels leads to particles being present in the furnace. Particles emit, absorb, and scatter radiation and therefore, they have to be considered and modeled in an appropriate way when performing radiative heat transfer calculations. Flame radiation in cylindrical furnaces has been investigated in studies demonstrating the importance for pulverized coal-fired furnaces of different parameters, such as the scattering efficiencies of different particle types, concentrations, and size distributions [12] , as well as the temperature distribution, extinction coefficients, and single-scattering albedo [13]. The importance of using separate temperatures for gases and particles has also been evaluated [14]. In these studies, it was found that coal and char particles were the main contributors to the heat flux at the wall, and the importance of scattering was underlined [12]. It was concluded that for predicting the radiative heat transfer in a coal-fueled furnace, a thorough understanding of the temperature and particle concentration distributions was more critical than detailed information on the gas concentration or the index of refraction [14].

To calculate the radiative properties of particles, the Mie theory is usually applied for larger particles and the Rayleigh theory is used for smaller particles [5]. Radiation is emitted from the surfaces of the particles, and the size of the particles affects the scattering. Even if the fuel that is fed to the burner has a narrow size distribution, the particles will start to combust and the size distribution will change over time in the furnace, which has to be considered. To reduce $CO_2$ emissions from combustion processes, co-firing of coal and biomass is of interest and for such cases, the particle distribution may vary over a wide size range. An example of particles that were collected from a co-firing flame (Figure 16) clearly shows the broad range of particle sizes.

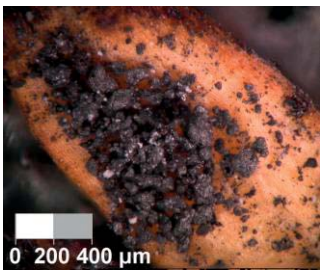


**Figure 16.** Particles collected from a co-firing flame. The white biomass particle is clearly much larger than the black coal particles.

It should be noted that a solid fuel flame contains not only fuel particles, but also ash and soot particles, all of which have different properties. In addition, in gaseous flames, soot particles

may form and should be taken into account. In this work, in considering the material, we differentiate between fuel, ash, and soot particles, although all the particles are treated as spheres For a cloud of spherical particles with radius *a,* the radiative properties for an interacting ray of light are given by three dimensionless parameters: the *complex index of refraction*; a *size parameter*; and the *clearance-to-wavelength ratio,* as shown in order in Eqn. (13).

$$m_\lambda = n_\lambda - ik_\lambda$$

$$x = 2\pi a/\lambda \tag{13}$$

$$c/\lambda$$

The clearance-to-wavelength ratio has been shown to be of no importance in cases where the ratio is >0.5 [43], which is the case for almost all heat transfer problems. Therefore, this parameter is ignored in this work, and the scattering is deemed to be independent.

### *5.2.1 Mie theory*

The Mie theory, which was developed by Gustav Mie, describes the radiative scattering of light by spherical particles. While the theory is complex, it basically means that the Maxwell equations are solved for an electromagnetic wave travelling through a medium that contains a sphere. In this work, the Mie theory is used for particles of ash and fuel. The theory generates absorption and scattering coefficients, calculated from the respective efficiency factors, $Q_{abs}$ and $Q_{sca}$, and the projected surface areas of the particles, $A_{proj}$:

$$\kappa = Q_{abs}A_{proj}$$

$$\sigma_s = Q_{sca}A_{proj} \tag{14}$$

The efficiency factors are calculated in this work using the derivations of Hulst [44] or Bohren and Huffman [45]. The absorption efficiency factor is calculated from the extinction and scattering efficiency factors such that:

$$Q_{abs} = Q_{ext} - Q_{sca}$$

$$Q_{sca} = \frac{2}{x^2}\sum_{n=1}^{\infty}[(2n+1)(|a_n|^2 + |b_n|^2)] \tag{15}$$

$$Q_{ext} = \frac{2}{x^2}\sum_{n=1}^{\infty}[(2n+1)(\mathbb{R}\{a_n\} + \mathbb{R}\{b_n\})]$$

where $n$ is an integer for an infinite series, and the complex numbers $a_n$ and $b_n$ are the Mie scattering coefficients [44], as functions of the complex refractive index. Although the series are infinite, it is not necessary to calculate the sum for a value of $n$ that is larger than a value termed $n_{max}$. As the $n$-value exceeds the value of the size parameter $x$ by 2 or 3, the contribution to the sum is negligible [44]. The stop criterion used in this work is from the work of Bohren and Huffman [45].

$$n_{max} = x + 4x^{1/3} + 2 \tag{16}$$

The wavelength-dependent refractive indices of the coal particles are in this work fitted to the data from Foster and Howarth [46], Table 2.

**Table 2.** Refractive indices used for coal particles

| $n_\lambda$ | [μm] | $k_\lambda$ |
|---|---|---|
| $1.67 + 0.033\lambda$ | $\lambda < 5$ | $k_\lambda = 0.3$ |
| | $5 \leq \lambda < 10$ | $k_\lambda = -0.5 + 0.16\lambda$ |
| | $10 \leq \lambda$ | $k_\lambda = 1.1$ |

Complex refractive indices for the ash particles, as functions of the radiation wavelengths, are collected from a function on combined data from the works of Lohi et al. [47] (0.6-2.6μm), Gupta and Wall [48] (2.6-5μm) and Goodwin and Mitchner [49] (> 5μm), Table 3.

**Table 3.** Refractive indices used for ash particles

| $[\mu m]$ | $n_\lambda$ | $[\mu m]$ | $k_\lambda$ |
|---|---|---|---|
| $\lambda < 6$ | 1.5 | $\lambda < 2.6$ | $-0.0015 + 7.5 * 10^{-3}\lambda$ |
| $6 \leq \lambda < 8$ | $1.5 - 0.35(\lambda - 6)$ | $2.6 \leq \lambda < 5$ | $0.0119 + 2.33 * 10^{-3}\lambda$ |
| $8 \leq \lambda < 11$ | $0.8 + 0.5(\lambda - 8)$ | $5 \leq \lambda < 9$ | $-1.19 + 0.244\lambda$ |
| $11 \leq \lambda < 12$ | $2.3 - 0.5(\lambda - 11)$ | $9 \leq \lambda < 11$ | 1.0 |
| $12 \leq \lambda$ | 1.8 | $11 \leq \lambda < 12$ | $8.7 - 0.7\lambda$ |
| | | $12 \leq \lambda$ | 0.3 |

*5.2.2 Rayleigh theory*

For particles that are much smaller than the radiated wavelengths, scattering is negligible and the particle properties can be calculated using the Rayleigh theory [5]. Neglecting the scattering, the RTE for the particles can be described in the same manner as in Eqn. (4), albeit for particles. Using the Rayleigh theory, the absorption coefficient can be calculated from the volume fraction of the soot particles rather than the size of the particles. With the refractive indices of the soot particles, the absorption coefficient can be calculated as:

$$\kappa_\lambda = E(m_\lambda)\frac{6\pi f_v}{\lambda} \tag{17}$$

where $f_v$ is the volume fraction of soot, $\lambda$ is a given wavelength, and $E(m_\lambda)$ is a function of the complex refractive index of soot $m_\lambda$, such that:

$$E(m_\lambda) = -Im\left[\frac{(m_\lambda^2 - 1)}{(m_\lambda^2 + 2)}\right] = \frac{6n_\lambda k_\lambda}{(n_\lambda^2 - k_\lambda^2 + 2)^2 + 4n_\lambda^2 k_\lambda^2} \tag{18}$$

The complex refractive index, $m_\lambda$, is given as in Eqn. (13). Wavelength-dependent functions of the complex refractive indices have been developed for the soot particles by Stull & Plass [50], Dalzell & Sarofim [51], Lee & Tien [52] and Chang & Charalampopoulos [53]. More recent

studies, however, claim that wavelength dependency on the $E(m_\lambda)$-function is low, or may even be ignored. Coderre et al. [54] have suggested that the function value is remarkably constant at around 0.35, in the wavelength range of 450–750 nm. However, in the present work, the complex refractive indices derived from Chang & Charalampopoulos [53] were used for the soot particle properties:

$$\begin{aligned} n_\lambda &= 1.811 + 0.1263 \ln \lambda + 0.027 \ln^2 \lambda + 0.0417 \ln^3 \lambda \\ k_\lambda &= 0.5821 + 0.1213 \ln \lambda + 0.2309 \ln^2 \lambda + 0.01 \ln^3 \lambda \end{aligned} \tag{19}$$

## 5.3 Gas and Particle Interactions

In the furnace, gases and particles co-exist and interact with each other. Using the Mie theory for ash and fuel particles and the Rayleigh theory for soot particles, the total particle absorption and scattering coefficients may be calculated at a point as the sum of the coefficients for the different particle types:

$$\begin{aligned} \kappa_\lambda &= \kappa_{\lambda,coal} + \kappa_{\lambda,ash} + \kappa_{\lambda,soot} \\ \sigma_{s\lambda} &= \sigma_{s\lambda,coal} + \sigma_{s\lambda,ash} \end{aligned} \tag{20}$$

The particle absorption and scattering coefficients can be used to calculate transmissivity along a distance *s*:

$$\tau_{\lambda,p} = e^{(-(\kappa_\lambda + \sigma_{s\lambda})s)} \tag{21}$$

The total transmissivity can be calculated as the product of the transmissivities for the different gases and particles:

$$\tau_{\nu_k} = \tau_{\nu_k,g} \tau_{\nu_k,p} \tag{22}$$

Gray particle properties can be calculated from the spectral properties and used in a gray model:

$$\begin{aligned} \kappa_{grey,particles} &= \frac{1}{I_b} \sum \Delta\nu I_\nu \kappa_\nu \\ \sigma_{s,grey,particles} &= \frac{1}{I_b} \sum \Delta\nu I_\nu \sigma_{s\nu} \end{aligned} \tag{23}$$

## 5.4 Furnace Modeling

Calculation of the radiative intensity field in a furnace requires a model in which the different types of radiation, absorption, and scattering (as discussed above) are included. The furnaces examined in this work are cylindrical furnaces and therefore, models of cylindrical enclosures are discussed in the following sections. Two different models are described, namely the *discrete transfer model* and the *discrete ordinates method.* Both of these models employ the $S_N$-approximation and discrete ordinates to identify appropriate and weighted rays of intensities.

The input data required by the radiation models are mainly the radial profiles of temperature, gas composition, projected surface area of the fuel and ash particles, and the soot volume fraction. The model outputs of major interest are the radiative intensities from the gases and soot particles (separately) and the total intensity, as well as the heat fluxes to the furnace wall.

The total radiative intensity corresponds to the intensity measured with the narrow angle radiometer and the modeled radiative heat flux corresponds to the heat flux measured using the ellipsoidal radiometer (see Section 4).

### *5.4.1 $S_N$-approximation*

The directions of the intensity rays are in this work set using directions derived according to an $S_N$-approximation. The $N$ denotes the number of different direction cosines used for each principal direction, such that the total number of directions is given by: $N \cdot (N+2)$. The models used in this work include options whereby the rays can be distributed according to their $S_4$-, $S_6$- or $S_8$-approximations. Each direction is given by the direction cosines $\xi_i, \eta_i$ and $\mu_i$ for a ray travelling along the discrete direction $\hat{\boldsymbol{s}}_i$ according to Eqn. (24) and Figure 17 [55], [56].

$$\hat{\boldsymbol{s}}_{\boldsymbol{i}} = \xi_i \hat{\boldsymbol{\imath}} + \eta_i \hat{\boldsymbol{\jmath}} + \mu_i \hat{\boldsymbol{k}}$$
$$\xi_i^2 + \eta_i^2 + \mu_i^2 = 1 \tag{24}$$

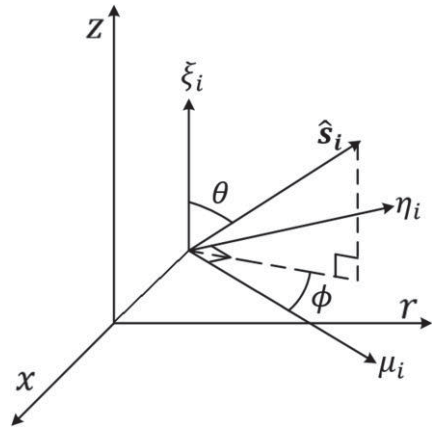


$$\xi_i = \cos\theta$$
$$\eta_i = \sin\theta \sin\phi$$
$$\mu_i = \sin\theta \cos\phi$$

**Figure 17.** The direction cosines ($\xi_i, \eta_i$ and $\mu_i$) for the discrete direction $\hat{s}_i$ in a cylinder

where $\theta$ and $\phi$ are the polar and azimuthal angles, respectively. To cover the whole sphere from a point, of 4π sr, the ordinates may be positive or negative. The directions given in the one-eighth part of a full sphere, where all the ordinates are positive, are given for the S4-approximation in. All other directions are given by altering the combination of positive or negative signs in front of the ordinates, resulting in eight directions for each row.

**Table 4.** Discrete ordinates for the S4-approximation

| Order of Approximation | Ordinates | | | Weights |
|---|---|---|---|---|
| | $\xi$ | $\eta$ | $\mu$ | $w$ |
| S4 | 0.2958759 | 0.2958759 | 0.9082483 | 0.5235987 |
| | 0.2958759 | 0.9082483 | 0.2958759 | 0.5235987 |
| | 0.9082483 | 0.2958759 | 0.2958759 | 0.5235987 |

For values of the discrete cosines and weights for the $S_6$- and $S_8$-approximations, see the work of Modest [5]. Each set of ordinates is also connected to a weight, $w$, such that:

$$\sum_{i}^{N}(\xi_i^2 + \eta_i^2 + \mu_i^2) \cdot w_i = 4\pi\ sr \tag{25}$$

when both positive and negative signs of the cosine directions are considered.

*5.4.2 Discrete transfer model*

The discrete transfer model was developed to solve the RTE for representative rays of intensity in a volume by tracing the rays that are travelling from one surface to another in predetermined directions. The model was first developed by Lockwood and Shah [57] , who tested the model for one-, two-, and three-dimensional problems and found a good accordance to analytical solutions and to solutions generated using the Monte Carlo method. The rays used were set to be directed to a point, so that they were distributed angularly in an equal fashion in space. In this work, the furnace is treated as an infinitely long cylinder with axisymmetric properties within the discrete transfer model [58]. That is, the temperatures, as well as the gas and particle concentrations are symmetrically distributed around the axis of the furnace and there are no gradients in the axial direction. The rays are directed according to the $S_N$-approximations. However, when tracing a ray through the center position in an axisymmetric cylindrical furnace, it is only necessary to make the calculation for rays in one-fourth of a hemisphere. Thus, when tracing a ray in either the forward or backward direction, the number of rays that need to be considered is decreased to: $N \cdot (N+2)/8$.

The radiative intensity is calculated along a number of grid points set between the furnace wall and center position. Rays from the directions given by the $S_N$-approximation, crossing the grid points, are traced and the total number of rays in the model is equal to the number of grid points times the number of rays in each point [58]. The grid-point discretization of the path can be illustrated as shown in Figure 18.

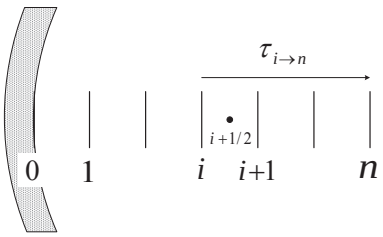


**Figure 18.** Discretisation of the radiative path in the discrete transfer model

As the ray is traced, the intensity at cell node *n*, $\bar{I}_{\nu_k,n}$, is dependent on the emission of all upstream cells as well as the radiation leaving the wall. The intensity is calculated as a sum of the difference in transmissivity between the two cell walls of the same cell, along the path to *n*, multiplied with the spectral black body intensity, $\bar{I}_{b\nu}$. The model calculates gas properties using the Malkmus SNB model, and if only gases are present along the path the solution to the RTE for a narrow band *k* may be written according to Eqn. (26) at the end of the path, at position *n*:

$$\bar{I}_{\nu_k,n} = \bar{I}_{\nu_k,0}\bar{\tau}_{\nu_k,0\to n} + \sum_{i=0}^{n-1}\left(\bar{\tau}_{\nu_k,i+1\to n} - \bar{\tau}_{\nu_k,i\to n}\right)\bar{I}_{b\nu_k,i+½} \tag{26}$$

If particles are present along the path, the Mie theory is used for the fuel and ash particle properties and the Rayleigh theory for the soot particles. The solution to the RTE becomes more complex and may be written as:

$$\bar{I}_{\nu_k,n} = \bar{I}_{\nu_k,0}\bar{\tau}_{\nu_k,0\to n} + \sum_i \left( \left(1 - \bar{\omega}_{\nu_k,i+½}\right)\bar{I}_{b\nu_k,i+½} + \frac{\bar{\omega}_{\nu_k,i+½}}{4\pi} G_{k,i+½} \right) \left(\bar{\tau}_{\nu_k,i+1\to n} - \bar{\tau}_{\nu_k,i\to n}\right) \tag{27}$$

where $G$ is the intensity integrated over all directions, and $\bar{\omega}_{\nu k}$ is the scattering albedo given as:

$$\bar{\omega}_{\nu_k} = \frac{\bar{\sigma}_{s\nu_k,coal} + \bar{\sigma}_{s\nu_k,ash}}{\bar{\beta}_{\nu_k,coal} + \bar{\beta}_{\nu_k,ash} - \ln\left(\bar{\tau}_{\nu_k,g}\right)/\Delta s_{cell}} \tag{28}$$

where $\beta$ is the extinction coefficient ($\beta = \kappa + \sigma_s$) and $\Delta s_{cell}$ is the cell length. The total radiative intensity at position $n$ is then calculated as the sum of all the spectral intensities and the bandwidth of each band $k$:

$$I_{tot,n} = \sum_k \Delta\nu_k \bar{I}_{\nu_k,n} \tag{29}$$

The incident radiative heat flux to the furnace wall is calculated from the weighted sum of the intensities for the different directions, $i$, according to the $S_N$-approximation:

$$q_r = \sum_{i=1}^{N} I_i w_i \mu_i \tag{30}$$

*5.4.3 Discrete ordinates method*

As gradients along the furnace axis are not considered in the discrete transfer model, it may be of interest to study instead the entire cylindrical furnace using a 3D model. Developed from neutron transport by Carlson and Lathrop [59] , the discrete ordinates method has been used previously for the modeling of radiative heat transfer in cylindrical furnaces [56], [60], [61]. In this approach, the cylindrical furnace volume is divided into cells in the radial $r$, axial $z$, and angular $\psi$ directions, so that the total number of cells is given by Eqn. (31).

$$n_{tot} = n_r \cdot n_z \cdot n_\psi \tag{31}$$

An example of cell discretization for a cylindrical furnace is shown in Figure 19a. However, considering the rotary kiln used for iron ore pellets production, a bed of iron ore pellets is present in the full scale furnace, filling approximately 8%-12% of the furnace volume. If the bed is assumed to be evenly distributed along the axis of the furnace, and over the same angular angle, the bed can be represented by a flat surface (Figure 19b). The properties, such as gas composition, particle projected surface area, and temperature, are set at the cell nodes, while the properties of wall temperature and bed emissivity are set at the cell surface nodes, i.e., no assumptions of symmetry are required. Using the discrete ordinates method, the modeled furnace is not infinite and, hence, also has a bottom and a top end. One end with the burner and one acting as the stack where the gases leaves the furnace.

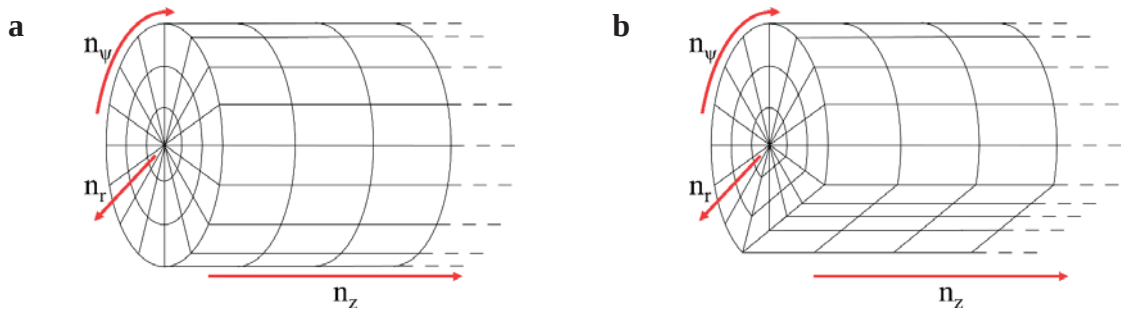


**Figure 19. a** Cell discretization of a cylindrical furnace. Considering the rotary kiln used for iron ore pellets production, a bed will be present and can be represented in the model according to **b**.

In contrast to the discrete transfer method, the radiative heat transfer is not traced along one discrete ray along the furnace diameter. The rays spread from the nodal points in the cells over the spheres, and calculations are performed for one sphere quadrant at a time. The quadrants are directed in each cell as shown in Figure 20, with each surface disc normal in the direction of either the axial or radial direction.

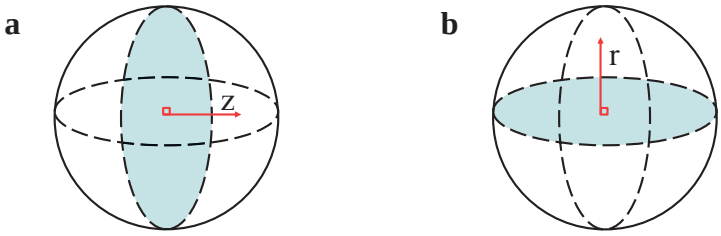


**Figure 20.** The orientation of the sphere quadrants using the discrete ordinates method. The normal for a disc, dividing the sphere, is in each cell directed along the axial direction **(a)** and radial direction (**b)**.

The heat transfer equation is solved in each discrete direction, which results in as many coupled partial differential equations, and an iterative process is required. The procedure starts at the outer wall at one end of the cylinder. Assumed values for the angular and reflected intensities are used in the first iteration and thereafter updated in each iteration. The WSGG model is used to model the gases in the furnace and the Mie and Rayleigh theories are used for the different particle types, while the gray properties are calculated for each cell according to Eqn. (23). The intensity to a node-point $P$ from one direction in a quadrant, with the beam directed from the wall to the furnace center, can be expressed as in Eqn. (32) [60].

$$I_{iP} = \frac{\mu_i A_A I_A + \eta_i A_B I_B + \xi_i A_C I_C + \frac{\alpha I_\alpha}{w_i} + (\kappa a_j I_b + \sigma_s I_{sca})V}{\mu_i A_A + \eta_i A_B + \xi_i A_C + \frac{\alpha}{w_i} + (\kappa + \sigma_s)V} \tag{32}$$

where α is used to correct for the curvature of the cylindrical furnace, $A_i$ represents the cell wall areas through which the radiation enters and leaves the cells, and $V$ is the cell volume. Using a model with a bed, two different cell types will be present, resulting in six different cell surfaces (Figure 21). Upstream intensities of $I_A$, $I_B$ and $I_C$ are calculated using a diamond scheme.

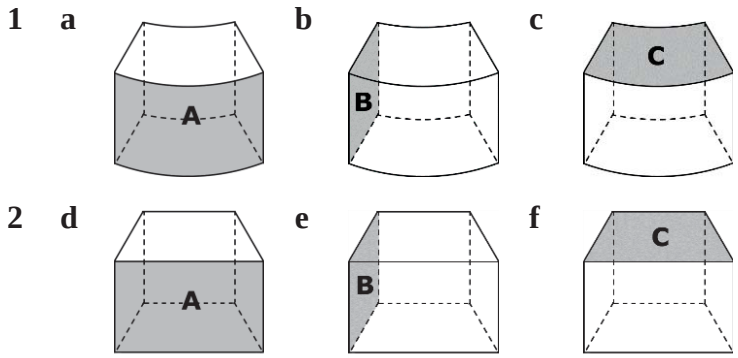


**Figure 21.** Representation of the two different cell types and surface areas present using the discrete ordinates method for a cylindrical furnace without (**a – c**) and with (**d – f**) a present bed material.

Each cell wall area may be calculated as:

$$A_{A1} = \frac{2\pi r \Delta z \psi}{2\pi} = r\Delta z\psi \qquad A_{A2} = \sqrt{r_{i,j}^2 + r_{i,j+1}^2 - 2r_{i,j}r_{i,j+1}\cos(\psi)}\,\Delta z$$

$$A_{B1} = \Delta r \Delta z \qquad A_{B2} = \Delta r \Delta z \tag{33}$$

$$A_{C1} = \frac{(r_{i+1}^2 - r_i^2)\psi}{2} \qquad A_{C2} = \frac{r_{i+1,j}r_{i+1,j+1}\sin(\psi)}{2} - \frac{r_{i,j}r_{i,j+1}\sin(\psi)}{2}$$

The cell volume may be calculated in the same way for the two cell types:

$$V = A_C \Delta z \tag{34}$$

The incident radiative heat flux to the furnace wall can be calculated from the sum of the incident radiations from all directions, as in Eqn. (30).

### *5.4.4 Parameter profiles*

Various parameters, such as the gas and particle temperatures, gas composition, particle surface area, and soot volume fraction, have to be introduced into the model. In the discrete transfer model, axisymmetry is assumed and radial profiles are introduced, whereas a value for each cell node may be set in the discrete ordinates method. These parameters have to be either measured or estimated in some way. For cells that are located at positions between the two measurement points, a linear average is used in both models. In this work, separate temperatures for the gases and particles were not measured and it was assumed that the particles have the same temperature as the surrounding gas, which is measured with suction pyrometers. For the radial temperature profiles, temperatures measured on each side of the furnace center, say the right-side and left-side, were used and the average was calculated considering the temperatures to the power of four.

$$\bar{T} = \left(\frac{T_{Right}^4 + T_{Left}^4}{2}\right)^{\frac{1}{4}} \tag{35}$$

For the experimental cases with a solid fuel flame, the particles were extracted at only the center positions in this work, mainly owing to time restrictions during the measurement campaigns.

However, the particle distribution has to be estimated from a single point. In this work, it was assumed that the particles were spread along the furnace diameter following different profiles. The profiles for which the particles were equally distributed over the furnace diameter were tested, and a cosine-function was employed to describe the distribution, as discussed in Paper I. The way in which the particle-projected surface area, $A_{proj}$, is distributed at a position $r$ on the furnace radius $R$ is described by the function:

$$\begin{aligned} 0 \le r \le R_f \qquad & A_{proj}(r) = f_{proj} \cdot \frac{R^2}{R_f^2} \cdot 1.681 \left( \cos\left( \frac{\pi \cdot r}{R_f} \right) + 1 \right) \\ R_f < r \le R \qquad & A_{proj}(r) = 0 \end{aligned} \tag{36}$$

where $R_f$, is the flame radius, i.e., the distance from the furnace center of the particles that are assumed to be present, and $f_{proj}$ is the projected surface area if the particles are equally distributed over the entire furnace diameter. Figure 22 shows three examples of particle distribution in a furnace with a radius of 325 mm. The three profiles depend on $R_f$, although the central peak value is constant, corresponding to the particle extraction measurements.

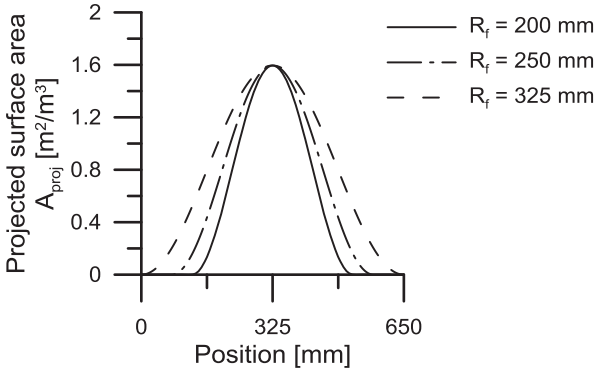


**Figure 22.** Example of particle distribution patterns over a furnace diameter of 650 mm using three different flame radii.

The flame radius can be revealed by studying the measurements of the radiative intensity along the furnace diameter. This is discussed further in Paper I.

### *5.4.5 Scattering*

Scattering occurs due to three reasons when radiation approaches a particle, either due to diffraction, reflection or refraction. The radiative scattering depends on multiple properties of the particle, such as the size, shape and the material of the particle [5]. However, as mentioned earlier, all particles are assumed to be spherical in this work. Though, it has been shown in the work by Gronarz et al. [62] that the particle shape is of little importance in terms of scattering. The scattering efficiency factor is calculated for coal and ash particles using the Mie theory for both the discrete transfer model and the discrete ordinates model. However, it is difficult to describe in a satisfactory way in the models the direction of the scattering from the particles. A commonly applied simplification is to assume that the scattering is isotropic, i.e., the scattering occurs equally in all directions. However, the scattering is usually much stronger in the forward direction of the incoming radiation [5]. To show this effect, a certain amount of the scattered

radiation was designated as being scattered forward, i.e., transmitted radiation, while the remaining part was scattered isotropically, using the discrete transfer model. The modeled case was a coal flame with particles distributed over the furnace diameter. A cold background was used to study the radiation from the flame and the in-scattered radiation from the surroundings. A colder furnace wall (at 500°C) was compared to a hotter one (at 1200°C) (Figure 23). It is clear from the results that the in-scattering has a greater impact on the radiative intensity when the furnace wall is hot.

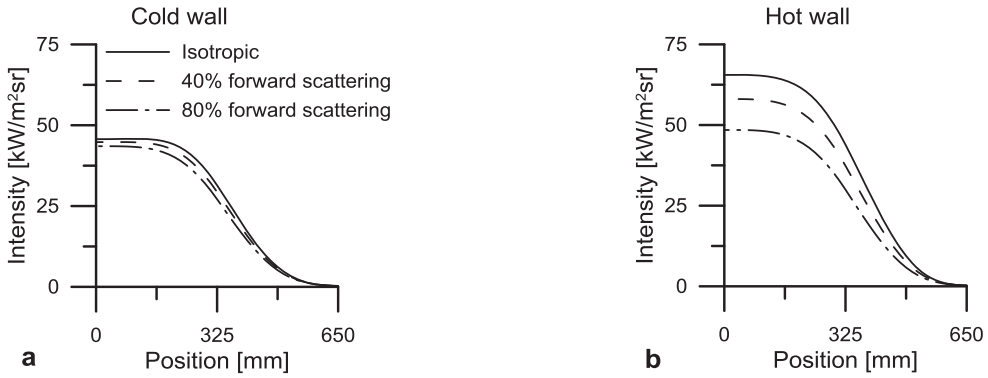


**Figure 23.** Variation of the portion of the incoming radiation that is forward-scattered (40% or 80%) compared to fully isotropic scattering for a flame with a solid fuel. The wall temperature is 500°C (**a)** or 1200°C (**b)**.

In our earlier works, scattering was assumed to be isotropic, which resulted in only minor errors (Figure 23a) for a colder furnace wall. However, for cases in which the furnace wall is heated, as in the rotary kiln furnace, the effects of the non-isotropic cases are considerably larger (Figure 23b). Therefore, further work is required to improve the modeling of the scattering due to particles in the radiation models. Moreover, the different types of particles warrant more detailed studies.

# 6. Results and Discussion

## 6.1 Radiative Heat Transfer in a Rotary Kiln Test Furnace

The ECF, as described in section 3, was used for two measurement campaigns designed to study the radiative heat transfer properties of the rotary kiln process. This thesis includes modeling results based on measurements from both campaigns. The measurements obtained in the earlier campaign in 2013 are used in Paper IV to compare the discrete transfer model with the discrete ordinates method, as well as to examine the axial heat flux profile. The measurements acquired during the more recent campaign in 2015 are evaluated and modeled more extensively in Paper I.

Regarding the later campaign, the radiative intensity was measured for the different fuels studied, but Paper I focuses only on the cases using the Svappavaara burner configuration. Comparing the measurements for the three fuel combinations, it is evident that the differences are minor, especially for the reference coal and the co-firing with biomass A, with the co-firing case with biomass B having slightly lower values at the different ports. The radiative intensities measured at port MH3 are shown in Figure 24. Measurements of the radiative intensity were performed by traversing the NAR along the furnace diameter at three of the measurement ports (MH1, MH3, and MH7) located axially from the burner (see Figure 5). The NAR probe entered the furnace at the 0-mm position, recording high radiative intensities because the entire furnace diameter with high concentrations of particles and hot gases is located in the line-of-sight of the detector. When the probe was traversed closer to the furnace center axis, the measured radiative intensity decreased because the number of particles in the line-of-sight between the probe and the cold background decreased. At the 650-mm position, at the opposite wall, the intensity was close to zero due to the presence of the quartz windows used as a cold background.

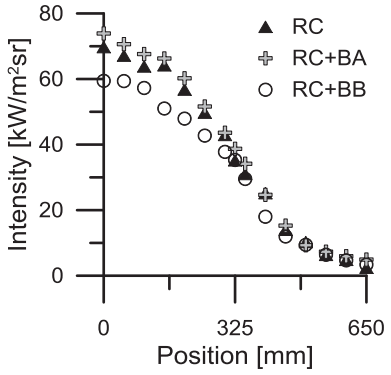


**Figure 24.** Measured radiative intensities at measurement port MH3 for the three fuel combinations tested in Paper I. RC, Reference coal; BA, biomass A (wood treated with steam explosion); BB, biomass B (ground and pelletized wood).

Measurements of temperature, gas composition and particle concentration were performed and used in the discrete transfer model to model the total radiative intensity. The measured (indicated with triangles) and modeled radiative intensity (lines) along the furnace diameter are

shown in Figure 25 for the co-firing case of the reference coal and biomass A. Comparing the axial ports, the measured radiative intensity increases moving from port MH1 to MH3, but decreases again moving downstream to port MH7. This is probably an effect of cold fuel particles that had yet not been ignited at port MH1, while the particles had been ignited to a greater extent at port MH3, which resulted in higher flame temperatures. At port MH7, the particle concentration is lower due to the progression of the combustion, and the contribution from particles to the radiative emission decreases. The gradient of the radiative intensity plots decreases along the furnace axis as the particles become more evenly distributed, i.e., when moving from port MH1 to MH3 and MH7. A comparison of the modeled contributions from gases and particles to the total radiative intensity reveals that particle radiation (dashed line) predominates and the fraction of the radiative intensity that arises from the gases (dash-dotted line) is small for all the cases and ports (Figure 25). Overall, the agreement between the measured and modeled radiative intensity is satisfactory for the different ports and cases. This implies that the measurements of temperature and particle concentrations were accurate in this campaign and were improved from the earlier campaign.

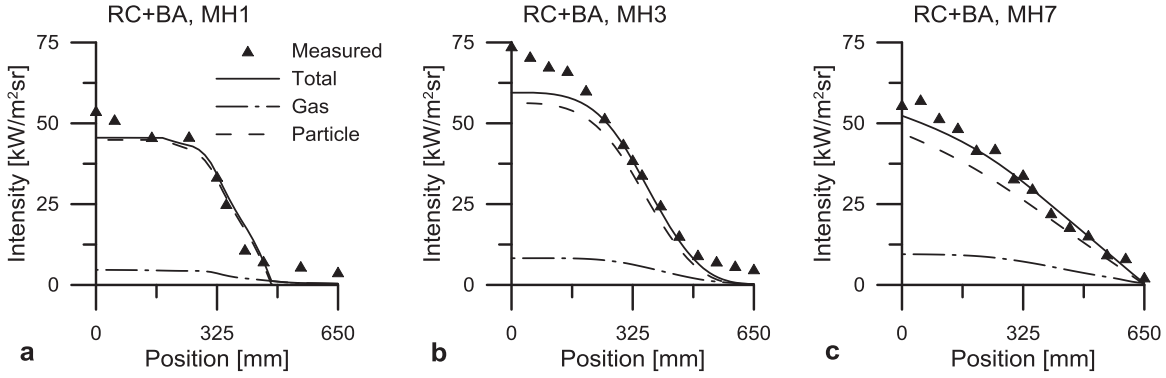


**Figure 25.** Measured and modeled radiative intensities for the co-firing case of the reference coal (RC) and biomass A (BA) performed during the ECF 2015 measurement campaign at ports: **a** MH1; **b** MH3; and **c** MH7.

During the 2015 campaign, the radiative heat flux to the inner wall of the furnace was measured for ports MH0, MH1, MH3, and MH7 for the three studied cases using the ellipsoidal radiometer. The radiative heat flux to the wall was modeled for ports MH1, MH3 and MH7, using the discrete transfer model and is shown together with the corresponding measured values in Figure 26. Since iron ore pellet quality is largely affected by the radiative heat transfer from the flame, the radiative heat flux directed to the wall of the furnace is an important parameter to study and understand. Figure 26 shows only small differences between the measured and modeled radiative heat fluxes at the ports close to the burner, MH1 and MH3, while the model over-estimates the heat flux at the downstream port MH7. Comparing the different fuel combinations, only minor differences are observed between the measurements for all the ports. This result raises the possibility of using co-firing in the full-scale rotary kiln, as the radial heat profile is similar for all fuels.

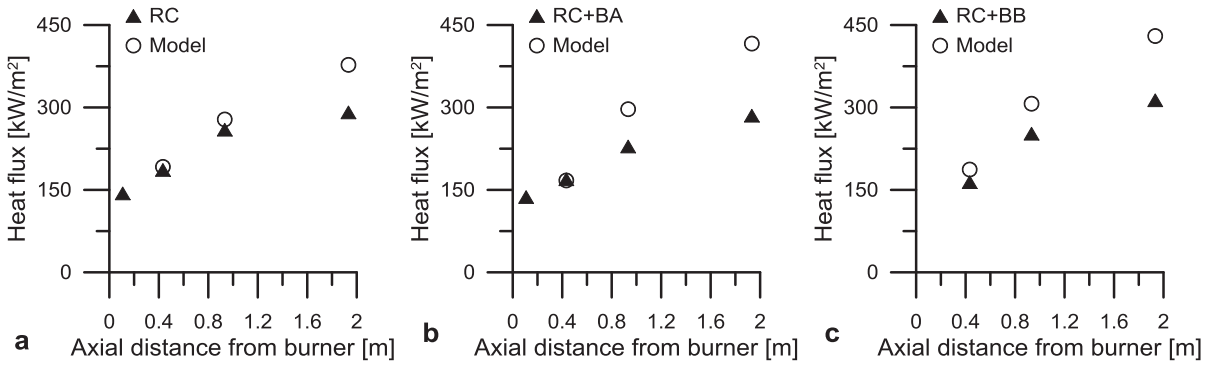


**Figure 26.** Measured and modeled radiative heat fluxes for the different fuels and measurement ports, **a** reference coal (RC); **b** co-firing with biomass A (BA), wood treated with steam explosion; and **c** co-firing with biomass B (BB), ground and pelletized wood.

Measurements obtained during the 2013 campaign were used in Paper IV, to model the incident heat flux to the furnace wall using the discrete ordinates method. The results shown here focus on the two different coals tested during that campaign. The two coals showed large differences in the measured radiative intensity, although they appeared to be very similar in the fuel analysis (Figure 27a). Radial profiles were inserted from measurements taken at axial locations corresponding to the measurement positions, and averaging was employed for the cells between the ports. The particle profiles were not measured but were assumed along the furnace axis. A cell resolution of 20×20×180 was used, and the results are shown in Figure 27b. While this is an early study using the discrete ordinates method, it may be observed that the radiative heat flux to the furnace wall is in agreement with the measured radiative intensity for the two different coals.

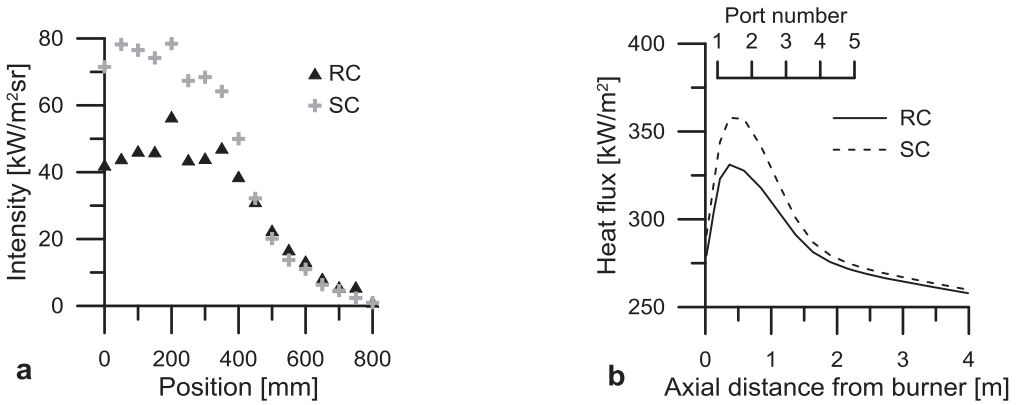


**Figure 27. a,** Measured radiative intensity for the reference coal (RC) and a similar coal (SC). **b,** The modeled incident radiative heat fluxes to the furnace wall along the furnace axis for the RC and SC.

## 6.2 Soot Formation in Propane Flames

The soot volume fractions in the propane flames were studied during the two measurement campaigns included in this thesis, using two different measurement methods. Both campaigns were conducted in the Chalmers 100-kW oxy-fuel test rig, as described in Section 3, using a thermal input of 80 kW of propane.

The first campaign was conducted in 2014 for two air/propane flames with an open and closed primary air register, respectively, as described in Paper III. The former flame appeared to have very few soot particles (non-sooty), while the latter flame was considered to be sooty. The absorption and scattering coefficients were measured for the soot particles using the PASS-3 instrument, as described in Section 4. Values for the absorption coefficients were compared to those in the literature [50]–[53] , and the results obtained at port M3 are shown in Figure 28 for the sooty flame. There was generally good agreement between the measured and modeled absorption coefficients, for all four models tested. To calculate the absorption coefficients with the models, the soot volume fraction is required. This was measured during the campaign using SMPS (see Section 4) and the soot volume fraction at port M3 was estimated to be about 65 ppb for the sooty flame.

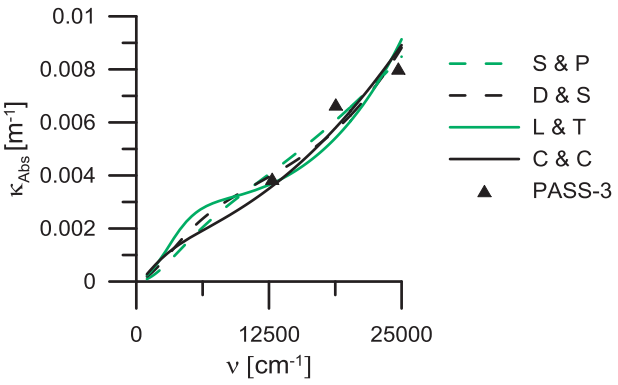


**Figure 28.** Measured values at port M3 of the absorption coefficients for soot particles compared to functions found in the literature in works of Stull and Plass (S & P) [50], Dalzell and Sarofim (D & S) [51], Lee and Tien (L & T) [52], and finally, Chang and Charalampopoulos (C & C) [53].

The second campaign, which was conducted in 2016, is described in Paper II. The soot volume fraction was measured using an extinction laser together with the LII system (see Section 4), for air, oxygen-enriched air, and oxy-fuel flames. The measured soot volume fractions from the different air (A), oxygen-enriched air (E), and oxy-fuel (OF) flames at port M3 are shown in Figure 29. Two different air flames were tested using an open (A1) and a closed (A2) primary air register. The air was then enriched with oxygen to generate oxygen concentrations of 25% (E25), 27% (E27), and 30% (E30), and the oxygen level was varied together with the flue gas recirculation rate to achieve oxygen concentrations of 30% (OF30), 35% (OF35), 40% (OF40), and 42% (OF43) for the oxy-fuel flames. The radial distance for which measurements were possible was limited by the size of the laser sheet and the width of the measurement port. The central axis of the furnace is located at the 0-mm position in the figure. The results show that there are clear increases in soot formation for the oxygen-enriched air and oxy-fuel flames as the oxygen concentration in the oxidant is increased above a certain value. Comparing the oxygen-enriched cases with the oxy-fuel cases, it can be observed that soot formation is increased along with the oxygen concentration in both cases, although a distinct shift in soot formation occurs at higher oxygen concentrations for the oxy-fuel flames. The formation of soot increases due to both thermal and chemical effects as the oxygen concentration is increased, whereas soot formation is suppressed by the carbon dioxide in the oxy-fuel cases.

This is in line with the findings of Du et al. [19] and Liu et al. [20] , and proceeds according to reactions R1 and R2

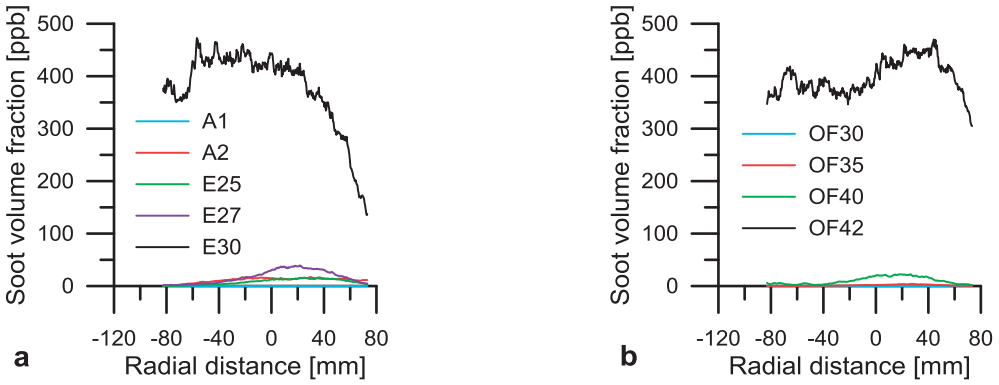


**Figure 29.** The measured soot volume fractions for: **a** air (A) and oxygen-enriched air (E) flames; and **b** oxy-fuel (OF) flames. A1 and A2 are the air flames created by a fully open and a fully closed primary air register, respectively. The numbers following the E and OF designations are the oxygen concentrations in the oxidant.

Together with the soot volume fractions, measurements of temperature and gas composition were performed and used to model the radiative intensity using the discrete transfer model. Modeling was performed in Papers II and III for air/propane and oxygen-enriched air/propane flames using the discrete transfer model. Good agreements were found for all flames with <30% oxygen in the oxidant. For flames with higher concentrations of oxygen, the measured radiative intensities were substantially higher. This may be due to higher flame temperatures or an increased soot volume fraction, which is in line with the measurements obtained using the LII system. However, the heavy particle loads clogged the suction pyrometer, resulting in the measured temperatures being erroneously low. As a consequence, the model to underestimated the radiative intensity (Figure 30a). When relying on measurements of the soot volume fraction, the model can instead be used to estimate the flame temperature. In an attempt to achieve a better fit between measured and modeled radiative intensity, the measured temperature values at the center of the flame were increased with 200°C in the model, which is in level with the temperature measurements for flames with a lower oxygen concentration (Figure 30b). As can be observed, a better match between modeling and experimental results was achieved.

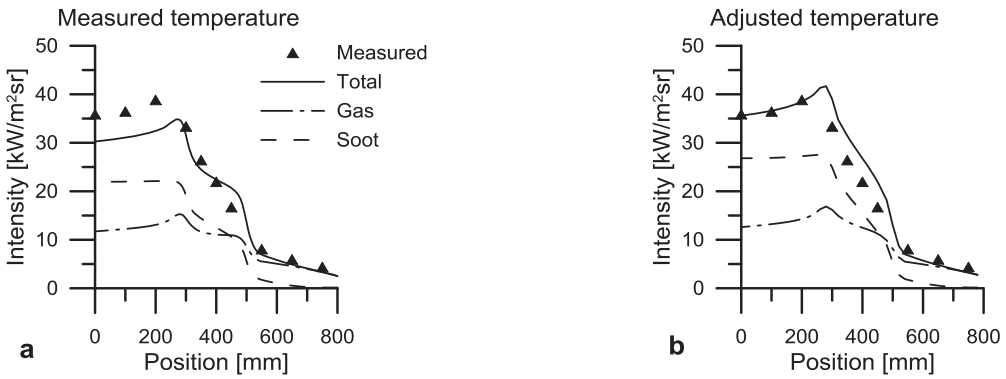


**Figure 30.** Measured and modeled radiative intensities for propane flames with 30% oxygen in the oxygen-enriched air used as the oxidant. **a**, Using measured temperature; and **b**, with an adjusted temperature profile.

# 7. Conclusions

The work presented in this thesis was carried out to examine the radiative heat transfer conditions in cylindrical furnaces, using both solid and gaseous fuels. Coal and co-firing flames were studied in a down-scaled version of a rotary kiln used for iron ore pellet production, using two different radiation models. The heat radiation from soot particles was studied in a propane flame by measuring the soot volume fraction using two different measurement techniques.

The possibility of co-firing coal and biomass to reduce greenhouse gas emissions without affecting the radiative heat profile is evaluated in Paper I. That paper focuses on three different fuels: a reference coal, and co-firing of the same reference coal with two different biomasses, biomass A, a wood treated with steam explosion, and biomass B, ground and pelletized wood. Comparing the measurements of the radiative heat flux and the radiative intensity, only minor differences were observed between the three cases. These similarities indicate the possibility to use biomass for co-firing in a rotary kiln used for iron ore pellet production while substantially lowering the carbon dioxide emissions without affecting the radiative heat transfer significantly. The cases were also modeled using the discrete transfer model, and good agreement was found between the measurements and the modeling results. This implies that the measurements were performed in an accurate way during the campaign, and that the model is a promising tool for reaching a better understanding of full-scale rotary kiln processes. The discrete ordinates method was used in Paper IV to study the radiative intensity and heat flux to the furnace wall using measurements from the campaign performed in 2013. Although rather crude assumptions of the different in-data parameters were used, the model exhibited satisfactory predictive qualities. While some development of the model is still required, the discrete ordinates method appears to be a promising tool for describing the radiative heat transfer in a full-scale rotary kiln process.

The soot volume fractions for different propane flames were studied and successfully measured (Papers II and III) in the Chalmers 100 kW oxy-fuel test rig. In both papers, the radiative intensity was modeled using the discrete transfer model, and good agreement was found between the measurements in both campaigns. By closing the primary air register, increased soot production could be observed for a propane/air flame using both the intrusive SMPS and non-intrusive LII measurement techniques. The soot volume fraction was also studied for flames that used oxygen-enriched air, and for cases in which the furnace was operated in oxy-fuel mode with different oxygen concentrations in the oxidant but retaining the stoichiometry. Soot formation was observed to increase in line with the oxygen concentration. Very steep increases in soot formation were observed, in excess of 27% and 40% for the oxygen-enriched air and oxy-fuel flames, respectively, increasing the soot volume fractions more than 10-fold compared to lower oxygen concentrations. The PASS-3 instrument was also used to study the soot particle properties. The absorption coefficients derived from the measurements showed trends towards good agreement with the models of the complex index of refraction used in the Rayleigh theory.

# 8. Suggestions for Future Work

During the experimental campaigns, severe problems were encountered with particle sampling. For flames with heavy particle loads at the sampling positions, the particles may clog the measurement probe, resulting in measurement errors. For co-firing flames, these problems are exacerbated by the presence of condensing tars. It is therefore of interest to continue the work of developing measurement techniques for particle extraction. Furthermore, the sampling process is time-consuming, so it is desirable to make the sampling process more time-efficient.

Connected to particle sampling is the importance of describing the radiative scattering in an appropriate way for coal-fired and co-firing flames, which has been addressed in this work. Isotropic scattering is a convenient simplification in the radiative heat transfer modeling and for a moderate-temperature furnace wall, the error appears to be small. However, the effect from in-scattering is much more significant when the furnace wall is hot, e.g., in applications such as the rotary kiln. It is therefore important to continue to develop the modeling, as well as to study experimentally the radiative scattering that occurs in combustion processes in the presence of particles.

So far, the down-scaled rotary kiln test furnace has been modeled using the two radiation models. The next step is to investigate radiative heat transfer in a full-scale rotary kiln that is used in an iron ore pellet plant. Measurements in the full-scale rotary kiln process should be planned to gain a better understanding of the process. Along with this, the discrete ordinates method model will be further developed and used to model the full-scale rotary kiln in three dimensions, including the pellets bed, and to examine the effects on radiative heat transfer of different parameter changes.

It would also be interesting to study in greater depth the rapid shifts in soot formation that were observed for the propane flames as the oxygen concentration was increased. The soot volume fraction was measured at one axial distance from the burner using the LII system during the latest campaign, and it would be of interest to study how it changes along the furnace axis.

# 9. Nomenclature

*Symbols*

| | |
|---|---|
| $a$ | particle radius [µm] |
| $a_j$ | weighting factor of gray gas *j* in the WSGG-model [-] |
| $a_n$ | Mie scattering coefficient [-] |
| $a_0$ | weighting factor of a clear gas in the WSGG-model [-] |
| $A$ | area [$m^2$] |
| $A_{proj}$ | projected particle surface area [$m^2m^{-3}$] |
| $b_n$ | Mie scattering coefficient [-] |
| $c$ | light velocity [$ms^{-1}$] |
| $c_{ij}$ | coefficient in the WSGG-model [-] |
| $C$ | coefficient in the WSGG-model [-] |
| $d_k$ | mean line spacing for a narrow band [$cm^{-1}$] |
| $f_{proj}$ | projected surface area [$m^2m^{-3}$] |
| $f_v$ | soot volume fraction [ppb] |
| $G$ | intensity integrated over all directions [$Wm^{-2}$] |
| $h$ | convective heat transfer coefficient [$Wm^{-2}K^{-1}$] |
| $\hat{\boldsymbol{\imath}}$ | unit vector [-] |
| $I$ | intensity [$Wm^{-2}sr^{-1}$] |
| $I_\nu$ | spectral intensity [$Wm^{-2}sr^{-1}$] |
| $I_0$ | incident intensity [$Wm^{-2}sr^{-1}$] |
| $\hat{\boldsymbol{\jmath}}$ | unit vector [-] |
| $k_k$ | mean line intensity to typical line spacing ratio within a narrow band [$cm^{-1}$] |
| $k_\lambda$ | absorptive index [-] |
| $\widehat{\boldsymbol{k}}$ | unit vector [-] |
| $K$ | coefficient in the WSGG-model [-] |
| $L$ | length [m] |
| $m_\lambda$ | complex index of refraction [-] |
| $n$ | integer / cell node / cell number [-] |
| $n_{max}$ | stop criterion used in Mie theory caculations [-] |
| $n_\lambda$ | refractive index [-] |
| $N$ | order of the $S_N$-approximation [-] |
| $P$ | total pressure [bar] |

| | |
|---|---|
| $q_r$ | radiative heat flux [$Wm^{-2}$] |
| $Q_{abs}$ | absorption coefficient [-] |
| $Q_{ext}$ | extinction coefficient [-] |
| $Q_{sca}$ | scattering coefficient [-] |
| $r$ | radius / radial distance [m] |
| $R$ | furnace radius [m] |
| $R_f$ | flame radius [m] |
| $s$ | coordinate along a radiative path [-] |
| $\hat{s}$ | unit vector in a given direction [-] |
| $S$ | total path length [m] |
| $S_l$ | line strength [-] |
| $T$ | temperature [K] |
| $V$ | volume [$m^3$] |
| $w$ | weight for a discrete ordinate [sr] |
| $x$ | size parameter [-] |
| $Y$ | mole fraction [-] |
| $z$ | axial distance [m] |

*Greek symbols*

| | |
|---|---|
| $\alpha$ | geometrical coefficient [-] |
| $\beta$ | extinction coefficient [$m^{-1}$] |
| $\gamma$ | mean line half-width [$cm^{-1}$] |
| $\Delta s_{cell}$ | length of computational cell [m] |
| $\Delta\nu$ | bandwidth [$cm^{-1}$] |
| $\varepsilon$ | emissivity [-] |
| $\eta$ | direction cosine [-] |
| $\theta$ | polar angle [rad] |
| $\kappa$ | absroption coefficient [$m^{-1}$] |
| $\kappa_\nu$ | spectral absorption coefficient [$m^{-1}$] |
| $\lambda$ | wavelength [µm] |
| $\lambda_d$ | diode laser wavelength [µm] |
| $\mu$ | direction cosine [-] |
| $\nu$ | wavenumber [$cm^{-1}$] |
| $\xi$ | direction cosine [-] |

| | |
|---|---|
| $\sigma$ | stefan Bolzmann constant [$Wm^{-2}K^{-4}$] |
| $\sigma_{sv}$ | spectral scattering coefficient [$m^{-1}$] |
| $\tau$ | transmissivity [-] |
| $\Phi_v$ | spectral scattering phase function [$sr^{-1}$] |
| $\phi$ | azimuthal angle [rad] |
| $\Psi$ | rotational angle [rad] |
| $\Omega_i$ | solid angel [sr] |
| $\omega$ | scattering albedo [-] |

*Subscripts*

| | |
|---|---|
| $b$ | black body |
| $d$ | diode laser |
| $g$ | gas |
| $i$ | cell number / cosine direction number |
| $j$ | gray gas number |
| $k$ | narrow band number |
| $p$ | particle |
| $P$ | node point |
| $tc$ | thermocouple |

# 10. Bibliography


[1] A. A. Boateng, *Rotary Kilns Transport Phenomena and Transport Processes*. Burlington, 2008.

[2] H. C. Hottel and A. F. Sarofim, *Radiative Transfer*. United States of America: McGraw-Hill, Inc., 1967.

[3] R. Siegel and J. R. Howell, *Thermal Radiation Heat Transfer*. United States of America: McGraw-Hill, Inc., 1972.

[4] M. N. Özisik, *Radiative Transfer and Interactions with Conduction and Convection*. United States of America: John Wiley & Sons, Inc., 1973.

[5] M. F. Modest, *Radiative Heat Transfer*, Third. United States of America: Elsevier, 2013.

[6] D. Bäckström, R. Johansson, K. Andersson, F. Johnsson, S. Clausen, and A. Fateev, "Gas Temperature and Radiative Heat Transfer in Oxy-Fuel Flames," Paper presented at 37th International Technical Conference on Clean Coal & Fuel Systems. The Clearwater Clean Coal Conference, Clearwater, FL, United States. **2012**.

[7] D. Bäckström, R. Johansson, K. Andersson, F. Johnsson, S. Clausen, and A. Fateev, "Measurement and modeling of particle radiation in coal flames," *Energy and Fuels*, vol. 28, no. 3, pp. 2199–2210, 2014.

[8] D. Bäckström, D. Gall, M. Pushp, R. Johansson, K. Andersson, and J. B. C. Pettersson, "Particle composition and size distribution in coal flames – The influence on radiative heat transfer," *Exp. Therm. Fluid Sci.*, vol. 64, pp. 70–80, 2015.

[9] D. Bäckström, R. Johansson, K. Andersson, H. Wiinikka, and C. Fredriksson, "On the use of alternative fuels in rotary kiln burners — An experimental and modelling study of the effect on the radiative heat transfer conditions," *Fuel Process. Technol.*, vol. 138, pp. 210–220, 2015.

[10] U.S. Geological Survey, "MINERAL COMMODITY SUMMARIES 2016," 2016.

[11] C. Y. C. Jonsson, J. Stjernberg, H. Wiinikka, B. Lindblom, D. Boström, and M. Öhman, "Deposit formation in a grate-kiln plant for iron-ore pellet production. Part 1: Characterization of process gas particles," *Energy and Fuels*, vol. 27, no. 10, pp. 6159–6170, 2013.

[12] J. G. Marakis, C. Papapavlou, and E. Kakaras, "A parametric study of radiative heat transfer in pulverised coal furnaces," *Int. J. Heat Mass Transf.*, vol. 43, no. 16, pp. 2961–2971, 2000.

[13] M. P. Mengüc and R. Viskanta, "A Sensitivity Analysis for Radiative Heat Transfer in a Pulverized Coal-Fired Furnace," *Combust. Sci. Technol.*, vol. 51, pp. 51–74, 1987.

[14] B. W. Butler, M. K. Denison, and B. W. Webb, "Radiation Heat Transfer in a Laboratory-Scale , Pulverized Coal-Fired Reactor," *Exp. Therm. Fluid Sci.*, vol. 9, pp. 69–79, 1994.

[15] J. P. Gorog, J. K. Brimacombe, and T. N. Adams, “Radiative heat transfer in rotary kilns,” *Metall. Trans. B*, vol. 12, no. 1, pp. 55–70, 1981.

[16] P. V. Barr, J. K. Brimacombe, and A. P. Watkinson, “A heat-transfer model for the rotary kiln: Part II. Development of the Cross-Section Model,” *Metall. Trans. B*, vol. 20, no. 3, pp. 403–419, 1989.

[17] A. A. Boateng and P. V. Barr, “A thermal model for the rotary kiln including heat transfer within the bed,” *Int. J. Heat Mass Transf.*, vol. 39, no. 10, pp. 2131–2147, 1996.

[18] H. Richter and J. B. Howard, “Formation of polycyclic aromatic hydrocarbons and their growth to soot - a review of chemical reaction pathways, ” *Prog. Energy Combust. Sci.,* vol. 26, no. 4–6. 2000.

[19] D. X. Du, R. L. Axelbaum, and C. K. Law, “The Influence of Carbon Dioxide and Oxygen as Additives on Soot Formation in Diffusion Flames,” *Twenty-Third Symp. Combust.*, pp. 1501–1507, 1990.

[20] F. Liu, H. Guo, G. J. Smallwood, and Ö. L. Gülder “The Chemical Effects of Carbon Dioxide as an Additive in an Ethylene Diffusion Flame : Implications for Soot and NOx Formation,” *Combust. Flame*, vol. 125, pp. 778–787, 2001.

[21] T. R. Barfknecht, “Toxicology of soot,” *Prog. Energy Combust. Sci.*, vol. 9, no. 3, pp. 199–237, 1983.

[22] J. M. Samet, F. Dominici, F. C. Curriero, I. Coursac, and S. L. Zeger, “Fine Particulate Air Pollution and Moratlity in 20 U.S. Cities, 1987-1994,” *N. Engl. J. Med.*, vol. 343, no. 24, pp. 1742–1749, 2000.

[23] R. Viskanta and M. P. Mengüc, “Radiation heat transfer in combustion systems,” *Prog. Energy Combust. Sci.*, vol. 13, no. 2, pp. 97–160, 1987.

[24] K. Andersson, R. Johansson, F. Johnsson, and B. Leckner, “Radiation Intensity of Propane-Fired Oxy-Fuel Flames: Implications for Soot Formation,” *Energy & Fuels*, vol. 22, no. 3, pp. 1535–1541, 2008.

[25] D. Bäckström, A. Gunnarsson, D. Gall, X. Pei, R. Johansson, K. Andersson, R. Kant Pathak, and J. B. C. Pettersson, “Measurements of the size distribution, volume fraction and optical properties of soot in an 80 kW propane flame,” Submitted for publication in Combustion and Flame, 2017.

[26] R. Edland, F. Normann, C. Fredriksson, and K. Andersson, “Implications of Fuel Choice and Burner Settings for Combustion Efficiency and $NO_x$ Formation in PF-Fired Iron Ore Rotary Kilns,” *Energy & Fuels*, vol. 31 no. 3, pp. 3253-3261, 2017.

[27] S. Hjärtstam, R. Johansson, K. Andersson, and F. Johnsson, “Computational fluid dynamics modeling of oxy-fuel flames: The role of soot and gas radiation,” *Energy and Fuels*, vol. 26, no. 5, pp. 2786–2797, 2012.

[28] K. Andersson, R. Johansson, S. Hjärtstam, F. Johnsson, and B. Leckner, “Radiation intensity of lignite-fired oxy-fuel flames,” *Exp. Therm. Fluid Sci.*, vol. 33, no. 1, pp. 67–76, 2008.

[29] P. R. Griffiths and J. A. Haseth, *Fourier Transform Infrared Spectrometry*, Second Edi.

John Wiley & Sons, Inc., 2007.

[30] W. Zhang, F. Johnsson, and B. Leckner, "Momentum probe and sampling probe for measurement of particle flow properties in CFB boilers," *Chem. Eng. Sci.*, vol. 52, no. 4, pp. 497–509, 1997.

[31] F. R. Quant, R. C. Flagan, and K. D. Horton, "Implementation of a Scanning Mobility Particle Sizer (SMPS)," *J. Aerosol Sci.*, vol. 24, no. 1, pp. 83–84, 1993.

[32] S. C. Wang and R. C. Flagan, "Scanning Electrical Mobility Spectrometer," *J. Aerosol Sci.*, vol. 20, no. 8, pp. 1485–1488, 1989.

[33] H. Moosmüller, R. K. Chakrabarty, and W. P. Arnott, "Aerosol light absorption and its measurement: A review," *J. Quant. Spectrosc. Radiat. Transf.*, vol. 110, no. 11, pp. 844–878, 2009.

[34] G. D. Yoder, P. K. Diwakar, and D. W. Hahn, "Assessment of soot particle vaporization effects during laser-induced incandescence with time-resolved light scattering.," *Appl. Opt.*, vol. 44, no. 20, pp. 4211–4219, 2005.

[35] R. L. Vander Wal and K. J. Weiland, "Laser-Induced incandescence: Development and characterization towards a measurement of soot-volume fraction," *Appl. Phys. B Laser Opt.*, vol. 59, pp. 445–452, 1994.

[36] B. Axelsson, R. Collin, and P. E. Bengtsson, "Laser-induced incandescence for soot particle size and volume fraction measurements using on-line extinction calibration," *Appl. Phys. B*, vol. 72, no. 3, pp. 367–372, 2001.

[37] H. Bladh, J. Johnsson, and P. E. Bengtsson, "On the dependence of the laser-induced incandescence (LII) signal on soot volume fraction for variations in particle size," *Appl. Phys. B Lasers Opt.*, vol. 90, no. 1, pp. 109–125, 2008.

[38] R. Johansson, B. Leckner, K. Andersson, and F. Johnsson, "Account for variations in the $H_2O$ to $CO_2$ molar ratio when modelling gaseous radiative heat transfer with the weighted-sum-of-grey-gases model," *Combust. Flame*, vol. 158, no. 5, pp. 893–901, 2011.

[39] R. M. Goody, "A statistical model for water-vapour absorption," *Quart. J. R. Meteorol. Soc.*, vol. 78, pp. 165–169, 1952.

[40] W. Malkmus, "Random Lorentz Band Model with Exponential-Tailed $S^{-1}$ Line-Intensity Distribution Function," *J. Opt. Soc. Am.*, vol. 57, no. 3, pp. 323–329, 1967.

[41] A. Soufiani and J. Taine, "High temperature gas radiative property parameters of statistical narrow-band model for $H_2O$, $CO_2$ and CO, and correlated-K model for $H_2O$ and $CO_2$," vol. 40, pp. 987–991, 1997.

[42] P. Rivière and A. Soufiani, "Updated band model parameters for $H_2O$, $CO_2$, CH4 and CO radiation at high temperature," *Int. J. Heat Mass Transf.*, vol. 55, no. 13–14, pp. 3349–3358, 2012.

[43] Y. Yamada, J. D. Cartigny, and C. L. Tien, "Radiative Transfer With Dependent Scattering by Particles : Part 2 — Experimental Investigation," vol. 108, pp. 614–618, 1986.

[44] H. C. van de Hulst, *Light Scattering By Small Particles*. New York: Dover Publications, 1981.

[45] C. F. Bohren and D. R. Huffman, *Absorption and Scattering of Light by Small Particles*. John Wiley & Sons, Inc., 1983.

[46] P. J. Foster and C. R. Howarth, "Optical Constants of Carbons and Coals in the Infrared," *Carbon N. Y.*, vol. 6, no. 5, pp. 719–729, 1968.

[47] A. Lohi, J. R. Wynnyckyj, and E. Rhodes, "Spectral measurement of the complex refractive index of fly ashes of canadian lignite and sub-bituminous coals," *Can. J. Chem. Eng.*, vol. 70, no. 4, pp. 751–758, 1992.

[48] R. P. Gupta and T. F. Wall, "The optical properties of fly ash in coal fired furnaces," *Combust. Flame*, vol. 61, no. 2, pp. 145–151, 1985.

[49] D. G. Goodwin and M. Mitchner, "Flyash Radiative Properties and Effects on Radiative Heat-Transfer in Coal-fired Systems," *Int. J. Heat Mass Transf.*, vol. 32, no. 4, pp. 627–638, 1989.

[50] V. R. Stull and G. N. Plass, "Emissivity of Dispersed Carbon Particles," *J. Opt. Soc. Am.*, vol. 50, p. 121, 1960.

[51] W. H. Dalzell and A. F. Sarofim, "Optical Constants of Soot and Their Application to Heat-Flux Calculations," *J. Heat Transfer*, vol. 91, p. 100, 1969.

[52] S. C. Lee and C. L. Tien, "Optical Constants of Soot in Hydrocarbon Flames," *Eighteenth Symp. Combust.*, pp. 1159–1166, 1981.

[53] H. Chang and T. T. Charalampopoulos, "Determination of the Wavelength Dependence of Refractive Indices of Flame Soot," *Proc. R. Soc. A Math. Phys. Eng. Sci.*, vol. 430, no. 1880, pp. 577–591, 1990.

[54] A. R. Coderre, K. A. Thomson, D. R. Snelling, and M. R. Johnson, "Spectrally resolved light absorption properties of cooled soot from a methane flame," *Appl. Phys. B Lasers Opt.*, vol. 104, no. 1, pp. 175–188, 2011.

[55] J. R. Tsai and M. N. Özişik, "Radiation in cylindrical symmetry with anisotropic scattering and variable properties," *Int. J. Heat Mass Transf.*, vol. 33, no. 12, pp. 2651–2658, 1990.

[56] A. S. Jamaluddin and P. J. Smith, "Predicting Radiative Transfer in Axisymmetric Cylindrical Enclosures Using the Discrete Ordinates Method," *Combust. Sci. Technol.*, vol. 62, no. 4–6, pp. 173–186, 1988.

[57] F. C. Lockwood and N. G. Shah, "A new radiation solution method for incorporation in general combustion prediction procedures," *Eighteenth Symp. Combust.*, pp. 1405-1414, 1981.

[58] R. Johansson, B. Leckner, K. Andersson, and F. Johnsson, "Influence of particle and gas radiation in oxy-fuel combustion," *Int. J. Heat Mass Transf.*, vol. 65, pp. 143–152, 2013.

[59] B. G. Carlson and K. D. Lathrop, "Transport Theory The Method of Discrete Ordinates," in *Computing Methods in Reactor Physics*, H. Greenspan, C. Kelber, and D. Okrent, Eds.

New York: Gordon and Breach Science Publishers, pp. 171–265, 1968.

[60] A. S. Jamaluddin and P. J. Smith, “Discrete-Ordinates Solution of Radiative Transfer Equation in Nonaxisymmetric Cylindrical Enclosures,” *J. Thermophys. Heat Transf.*, vol. 6, no. 2, pp. 242–245, 1992.

[61] M. Y. Kim and S. W. Baek, “Modeling of radiative heat transfer in an axisymmetric cylindrical enclosure with participating medium,” *J. Quant. Spectrosc. Radiat. Transf.*, vol. 90, no. 3–4, pp. 377–388, 2005.

[62] T. Gronarz, M. Schnell, C. Siewert, L. Schneiders, W. Schröder, and R. Kneer, “Comparison of scattering behaviour for spherical and non-spherical particles in pulverized coal combustion,” *Int. J. Therm. Sci.*, vol. 111, pp. 116–128, 2017.